J. Fluid Mech. (2021), *vol*. 913, A5, doi:10.1017/jfm.2020.1172

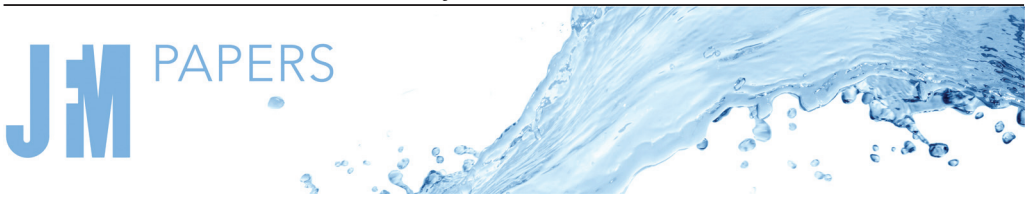

Instabilities of finite-width internal wave beams: from Floquet analysis to PSI

Boyu Fan[1] **and T.R. Akylas**[1],†

[1]Department of Mechanical Engineering, Massachusetts Institute of Technology, Cambridge, MA 02139, USA

(Received 23 July 2020; revised 27 November 2020; accepted 21 December 2020)

The parametric subharmonic instability (PSI) of finite-width internal gravity wave beams is revisited using a formal linear stability analysis based on Floquet theory. The Floquet stability eigenvalue problem is studied asymptotically in the limit where PSI arises, namely for a small-amplitude beam of frequency ω subject to fine-scale perturbations under nearly inviscid conditions. It is found that, apart from the two dominant subharmonic perturbation components with frequency $\omega/2$, PSI also involves two smaller components with frequency $3\omega/2$, which affect the instability growth rate and were ignored in the earlier models for PSI by Karimi & Akylas (*J. Fluid Mech.*, vol. 757, 2014, pp. 381–402) and Karimi & Akylas (*Phys. Rev. Fluids*, vol. 2, 2017, 074801). After accounting for these components, the revised PSI models are in excellent agreement with numerical solutions of the Floquet eigenvalue problem. The Floquet stability analysis also reveals that PSI is restricted to a finite range of perturbation wavenumbers: as the perturbation wavenumber is increased (for fixed beam amplitude), higher-frequency components eventually come into play due to the advection of the perturbation by the underlying wave beam, so the components at $\omega/2$ no longer dominate. By adopting a frame riding with the wave beam, this advection effect is factored out and it is shown that small-amplitude beams that are not generally susceptible to PSI may develop an essentially inviscid instability with broadband frequency spectrum.

Key words: internal waves

1. Introduction

The stability of internal gravity waves in a continuously stratified fluid is a problem of fundamental and geophysical interest. Early work focused on sinusoidal plane waves in an inviscid Boussinesq fluid with constant buoyancy frequency. In this idealized setting, linear stability analysis based on Floquet theory has revealed a wide host of instabilities

† Email address for correspondence: trakylas@mit.edu

with varying dynamics and physical mechanisms (e.g. see Sonmor & Klaassen (1997) and Yau, Klaassen & Sonmor (2004) for a comprehensive treatment). As first noted by Mied (1976), in the limit of small primary-wave amplitude, this diverse range of instabilities reduce to triad resonant interactions: the primary wave is unstable to two sinusoidal subharmonic perturbations whose frequencies and wavevectors sum to those of the basic state. A specific form of such triadic resonant instability (TRI), where the subharmonic perturbations have half the frequency of the primary wave and very fine wavelength, is the celebrated parametric subharmonic instability (PSI). This mechanism has attracted considerable interest as it permits transfer of energy into much smaller scales (e.g. Staquet & Sommeria 2002) and therefore may be a potentially significant factor in the dissipation of oceanic internal waves (Hibiya, Nagasawa & Niwa 2002; MacKinnon & Winters 2005; Young, Tsang & Balmforth 2008).

In more recent work, attention shifted from sinusoidal waves to time-harmonic plane waves with locally confined spatial profile: such wave beams arise in oceans due to the interaction of the barotropic tide with bottom topography (Lamb 2004; Cole *et al.* 2009; Johnston *et al.* 2011) and in the atmosphere due to thunderstorms (Fovell, Durran & Holton 1992), and therefore provide a more realistic setting for instability. However, compared with sinusoidal waves, formal stability analysis of wave beams based on Floquet theory is more demanding, as it requires solving an eigenvalue problem that involves an infinite number of differential, rather than algebraic, equations.

In view of this complication, Karimi & Akylas (2014) (hereafter referred to as KA14) proposed a simplified treatment of PSI assuming that two fine-scale subharmonic wave packets at half the beam frequency interact with a small-amplitude beam of locally confined profile. This model brings out the significance of the finite width of a beam: the subharmonic perturbations travel with their group velocity so, to cause instability, they must stay in contact with the beam long enough. By comparing the wavepacket travel time across the beam with the duration of resonant interaction in the beam vicinity, KA14 argued that small-amplitude finite-width beams generally are not susceptible to PSI. An exception arises when the beam profile is nearly monochromatic, in which case PSI is possible if the number of carrier wavelengths within the beam width is sufficiently large. The stabilizing effect of the finite width of a beam is also supported by laboratory experiments (Bourget *et al.* 2014), although the nearly inviscid flow scalings assumed in KA14 cannot be met in a laboratory setting. Furthermore, using a small-amplitude nearly inviscid model similar to that of KA14, Karimi & Akylas (2017) (henceforth referred to as KA17) showed that PSI is possible for beams with general spatial profile if the beam frequency $\omega \approx 2f$ (where f is the inertial frequency) because in this instance subharmonic perturbations with half the beam frequency are near-inertial and thus have nearly vanishing group velocity.

The original scope of the present investigation was to assess the validity of the PSI models of KA14 and KA17 by making a comparison with a formal linear stability analysis based on Floquet theory of small-amplitude wave beams under nearly inviscid flow conditions. In a recent related study, Onuki & Tanaka (2019) conducted a Floquet stability analysis of internal wave beams by exploiting the fact that the Floquet multipliers, which determine stability, are tied to the eigenvalues of the so-called monodromy matrix, which is easily computed by time integration. The emphasis of Onuki & Tanaka (2019), however, is on two- and three-dimensional instabilities of steep beams, far from the PSI regime considered in KA14 and KA17, so our intent was to fill this gap by applying the technique of Onuki & Tanaka (2019) to small-amplitude beams.

In carrying out this programme, we encountered difficulties obtaining quantitative agreement of the instability growth rates predicted by KA17 with those of the Floquet

stability analysis for near-inertial PSI. This led us to study afresh the Floquet stability eigenvalue problem in the limit pertinent to the models of KA14 and KA17, namely for a small-amplitude beam subject to fine-scale perturbations under nearly inviscid flow conditions. Our analysis confirms that the unstable Floquet mode in near-inertial PSI (beam frequency $\omega \approx 2f$) is dominated by two subharmonic wavepackets with carrier frequency $\omega/2$, as assumed in KA17; however, the two relatively small components of this mode at the frequency $3\omega/2$, which were ignored in KA17, also contribute to the stability eigenvalue problem and hence affect the instability growth rate. Once this contribution is taken into account, the predictions of the revised KA17 model are in excellent agreement with the Floquet stability analysis. A similar omission was also made in the PSI analysis of nearly monochromatic beams by KA14, but in this instance the $3\omega/2$ frequency components do not affect the instability growth rate, and the predictions of KA14 agree well with their Floquet stability counterparts.

Apart from bringing out the significance of the $3\omega/2$ frequency components in the PSI of wave beams, our asymptotic analysis of the Floquet eigenvalue problem also reveals that PSI, which assumes that the frequency components $\omega/2$ are dominant, is limited by how fine-scale the perturbations are for a given beam amplitude (assumed small). Specifically, as the perturbation wavenumber is increased holding the beam amplitude fixed, higher-frequency components eventually come into play. This broadening of the frequency spectrum of the Floquet mode was also noted in the numerical computations of Onuki & Tanaka (2019) and was attributed to the advection due to the underlying-beam velocity field. By adopting a frame riding with the wave beam, this advection effect is factored out and it is shown that small-amplitude beams with general (not necessarily nearly monochromatic) locally confined profile, which are not susceptible to PSI away from near-inertial conditions, may develop an essentially inviscid instability that features broadband frequency spectrum.

2. Floquet stability analysis

2.1. *General formulation*

The present analysis assumes an unbounded, incompressible, uniformly stratified Boussinesq fluid with constant buoyancy frequency N_* and includes the effect of background rotation under the f-plane approximation. Using non-dimensional variables with $1/N_*$ as the time scale and L_* as the length scale (to be specified later) the governing equations for the velocity field $\boldsymbol{u}$, the reduced density ρ and pressure p are

$$\boldsymbol{\nabla} \cdot \boldsymbol{u} = 0, \tag{2.1a}$$

$$\rho_t + \boldsymbol{u} \cdot \boldsymbol{\nabla} \rho = \boldsymbol{u} \cdot \boldsymbol{j}, \tag{2.1b}$$

$$\boldsymbol{u}_t + \boldsymbol{u} \cdot \boldsymbol{\nabla} \boldsymbol{u} + \boldsymbol{f} \times \boldsymbol{u} = -\boldsymbol{\nabla} p - \rho \boldsymbol{j} + \nu \nabla^2 \boldsymbol{u}. \tag{2.1c}$$

Here, $\boldsymbol{j}$ is a vertical unit vector pointing upwards, $\boldsymbol{f} = f\boldsymbol{j}$, where f is the local Coriolis parameter normalized with N_*, and $\nu = \nu_*/N_* L_*^2$ is the inverse Reynolds number, where ν_* denotes the kinematic viscosity.

In the inviscid limit ($\nu = 0$), (2.1) admits time-harmonic plane wave solutions in the form of beams (Tabaei & Akylas 2003) that feature general profile in the cross-beam (η) direction, and are uniform in the along-beam (ξ) and transverse horizontal (z) directions (figure 1*a*). Specifically, the beam velocity components (u, v, w) in the coordinate system

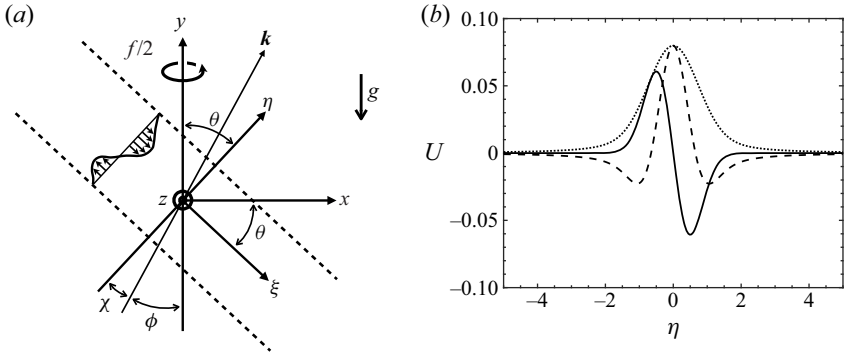

Figure 1. (*a*) Schematic of uniform beam with frequency ω and inclination θ to the horizontal, in keeping with (2.3). The coordinate system (ξ, η, z) is defined by the along-beam, cross-beam and transverse directions, respectively. Dotted lines indicate the finite width of the beam and the arrows within show the along-beam velocity u_0. The perturbation wavevector $\boldsymbol{k}$ is inclined by the angle χ to η and by $\phi = \theta - \chi$ to the vertical y. (*b*) Beam profile (3.1) for $\epsilon = 0.1$. Solid, dashed and dotted lines correspond to the real part, imaginary part and $|U|$, respectively.

(ξ, η, z), along with ρ and p, are given by

$$(u, v, w) = (u_0, 0, w_0) \equiv \left(1, 0, \frac{\mathrm{i}f\cos\theta}{\omega}\right) U(\eta)\mathrm{e}^{-\mathrm{i}\omega t} + \text{c.c.}, \tag{2.2a}$$

$$\rho = \rho_0(\eta, t) \equiv -\frac{\mathrm{i}\sin\theta}{\omega} U(\eta)\mathrm{e}^{-\mathrm{i}\omega t} + \text{c.c.}, \tag{2.2b}$$

$$p = p_0(\eta, t) \equiv \mathrm{i}(1-f^2)\frac{\sin\theta\cos\theta}{\omega}\int^{\eta} U(\eta')\,\mathrm{d}\eta'\mathrm{e}^{-\mathrm{i}\omega t} + \text{c.c.}. \tag{2.2c}$$

Here, the complex amplitude $U(\eta)$ specifies the beam profile and θ is the beam inclination angle to the horizontal (figure 1*a*), which is tied to the beam frequency ω via the (non-dimensional) dispersion relation

$$\omega^2 = f^2 + (1-f^2)\sin^2\theta. \tag{2.3}$$

Furthermore, (ξ, η) are related to the horizontal and vertical coordinates (x, y) by $\xi = x\cos\theta - y\sin\theta$ and $\eta = x\sin\theta + y\cos\theta$. Generally, finite viscosity ($\nu \neq 0$) will introduce along-beam variations in (2.2) (Mowbray & Rarity 1967; Thomas & Stevenson 1972). These viscous effects are ignored here.

The focus of the present analysis is on the stability of the primary wave (2.2) to infinitesimal perturbations. As (2.2) does not depend on ξ or z, we superimpose normal modes in the form

$$u = u_0 + \hat{u}(\eta, t)\exp(\mathrm{i}(\mu\xi + mz)), \tag{2.4}$$

where the real parameters μ and m specify the along-beam and transverse wavenumbers of the perturbation, with similar expressions for v, w, ρ and p. After inserting into (2.1) and linearizing with respect to the perturbations, we obtain the following equations (dropping

the hats):

$$0 = \mathrm{i}\mu u + v_\eta + \mathrm{i}mw, \tag{2.5a}$$

$$\rho_t = -\mathrm{i}(\mu u_0 + mw_0)\rho - \rho_{0\eta} v - u\sin\theta + v\cos\theta, \tag{2.5b}$$

$$u_t = -\mathrm{i}(\mu u_0 + mw_0)u - u_{0\eta} v - \mathrm{i}\mu p + \rho\sin\theta - wf\cos\theta + \nu\mathscr{L}u, \tag{2.5c}$$

$$v_t = -\mathrm{i}(\mu u_0 + mw_0)v - p_\eta - \rho\cos\theta - wf\sin\theta + \nu\mathscr{L}v, \tag{2.5d}$$

$$w_t = -\mathrm{i}(\mu u_0 + mw_0)w - w_{0\eta} v - \mathrm{i}mp + uf\cos\theta + vf\sin\theta + \nu\mathscr{L}w, \tag{2.5e}$$

where $\mathscr{L} \equiv -\mu^2 + \partial_\eta^2 - m^2$ takes into account the full effects of viscosity on the perturbations. As the basic state (2.2) is periodic in t (period $T_0 = 2\pi/\omega$), (2.5) is a linear equation system with periodic coefficients, which can be solved by Floquet theory to determine stability for a given beam profile $U(\eta)$ and parameters μ and m.

2.2. *Sinusoidal waves*

For a sinusoidal plane wave, the primary wave profile in (2.2) is taken in the form $U = \epsilon\exp(\mathrm{i}\eta)$, where the amplitude parameter $\epsilon = U_*/(N_* L_*)$, U_* being half the along-ξ velocity amplitude, and the wavelength has been normalized to 2π (which fixes the length scale L_*). In this instance, it is straightforward to solve (2.5) via Floquet theory by expanding the perturbations in Fourier series in $\eta - \omega t$, and thus recover the thoroughly studied instability of a sinusoidal plane wave (e.g. Sonmor & Klaassen 1997; Yau *et al.* 2004). Out of this body of work, of special interest here is the nearly inviscid ($\nu \ll 1$) small-amplitude limit ($\epsilon \ll 1$). In this regime, the most unstable perturbation is two-dimensional (i.e. $m = 0$) and involves only two subharmonic frequency components that are freely propagating sinusoidal internal waves and form a resonant triad with the primary wave. Specifically, these subharmonic waves, with frequencies (ω_1, ω_2) (where $|\omega_{1,2}| < \omega$) and wavevectors $(\boldsymbol{k}_1, \boldsymbol{k}_2)$, each satisfy the dispersion relation (2.3), and together satisfy the triad resonance conditions

$$\omega_1 + \omega_2 = \omega, \tag{2.6a}$$

$$\boldsymbol{k}_1 + \boldsymbol{k}_2 = \boldsymbol{k}_0, \tag{2.6b}$$

where $\boldsymbol{k}_0 = \hat{\boldsymbol{e}}_\eta$ is the primary wavevector. This class of instabilities, which encompasses all such pairs of $(\omega_1, \boldsymbol{k}_1)$ and $(\omega_2, \boldsymbol{k}_2)$, is thus known as TRI.

For inviscid flow conditions, in the event that the beam inclination angle $\theta \gtrsim 43^\circ$ for $f = 0$, or when $\omega \approx 2f$ for any θ, the most unstable pairs of subharmonic waves feature $\omega_1 \approx \omega_2 \approx \omega/2$ and $|\boldsymbol{k}_1| \approx |\boldsymbol{k}_2| \gg 1$ (e.g. Yeh & Liu 1981; Sonmor & Klaassen 1997). This particular form of TRI is widely known as PSI. However, it is important to note that other flow conditions may favour other forms of TRI over PSI. For instance, the most unstable triads for $\theta \lesssim 43^\circ$ and $f = 0$ involve subharmonic waves with $|\boldsymbol{k}_1| < 1 < |\boldsymbol{k}_2|$, which is sometimes referred to as the 'branch-C' instability (Sonmor & Klaassen 1997).

2.3. *Locally confined beams*

Moving away from the sinusoidal wave, KA14 and KA17 examined the possibility of PSI for locally confined beams in the small-amplitude nearly inviscid limit. As discussed in § 1, these approximate models of PSI are based upon the assumption of triad resonance, which strictly holds for a small-amplitude sinusoidal primary wave. Here, to assess the validity of KA14 and KA17, we perform a formal stability analysis of a locally confined

beam profile $U(\eta)$ based on the full stability problem (2.5). In general, this task has to be carried out numerically.

The stability problem (2.5) is more challenging to handle numerically for a general profile $U(\eta)$ than for the sinusoidal wave profile: in addition to Fourier expansion in t, it is necessary to use a separate discretization in η. To tackle this complication, we follow the approach taken by Onuki & Tanaka (2019) in their stability analysis of finite-amplitude internal wave beams under oceanic flow conditions. This approach was used earlier for inertial wave beams (Jouve & Ogilvie 2014) and also in a very recent study of finite-amplitude thin internal wave beams under laboratory flow conditions (Fan & Akylas 2020).

As our interest centres on the relevance of PSI to small-amplitude locally confined beams, we focus on two-dimensional perturbations ($m = 0$). It should be noted that three-dimensional ($m \neq 0$) instabilities are possible and may be important at large amplitudes (Onuki & Tanaka 2019). Furthermore, other three-dimensional instability mechanisms such as streaming, which involves the generation of a resonant mean flow due to finite transverse variations of a beam (Kataoka & Akylas 2015; Fan, Kataoka & Akylas 2018; Fan & Akylas 2020; Jamin *et al.* 2021) and thus falls beyond the scope of linear stability analysis, may be important in other contexts.

Following Onuki & Tanaka (2019), we solve (2.5) using the 'monodromy' matrix, which can be easily computed by integrating (2.5) over one period of oscillation of the primary wave, namely $T_0 = 2\pi/\omega$. The Floquet exponents $\lambda = \lambda_r + \mathrm{i}\lambda_i$, where $\lambda_r > 0$ implies instability, as well as the Floquet modes, are then obtained via the eigenvalues and eigenvectors of the monodromy matrix (see Fan (2020) and Fan & Akylas (2020) for details). Finally, we repeat this procedure for various μ in order to find the instability modes with the highest growth rate. In implementing this procedure, (2.5) was typically discretized using 1024 Fourier modes in the computational domain $\eta \in [-10, 10]$ and integrated using a pseudo-spectral method with fourth-order Runge–Kutta time stepping and a typical $\Delta t = 0.02$. The ensuing eigenvalue problem was then solved using standard MATLAB algorithms.

3. Floquet stability of beams with $\omega = 2f$

3.1. *Results*

To motivate the ensuing analysis (§ 4), we begin by considering finite-width beams in the presence of background rotation and attempt a comparison of the Floquet stability results with the predictions of the near-inertial PSI theory of KA17. This approximate model focuses on the resonant interaction between a small-amplitude wave beam with frequency $\omega \approx 2f$ and two subharmonic perturbations of frequency $\omega/2 \approx f$ and very fine wavelength. According to KA17, the vanishing group velocity of such near-inertial perturbations prolongs their interaction with the primary wave. As a result, when $\omega \approx 2f$, small-amplitude locally confined beams of general profile are susceptible to PSI in the nearly inviscid limit.

We present Floquet stability results for a small-amplitude beam with the Gaussian profile used in KA17, exactly at the critical frequency $\omega = 2f$ and for inviscid flow conditions ($\nu = 0$). Specifically, we chose $U(\eta)$ in (2.2) to be

$$U(\eta) = \frac{\epsilon}{\sqrt{8\pi}} \int_0^\infty \mathrm{i}l \mathrm{e}^{-l^2/8} \mathrm{e}^{\mathrm{i}l\eta} \mathrm{d}l \tag{3.1}$$

and set $\omega = 0.1$. Here, the non-dimensional amplitude parameter $\epsilon = U_*/N_*L_*$, where U_* and L_* are a characteristic (dimensional) velocity and width, respectively, of the primary wave beam. Combined with (2.2), the profile (3.1) (figure 1*b*) corresponds to a unidirectional (progressive) wave beam that transports energy in the positive ξ direction (figure 1*a*).

Figure 2(*a*) plots the computed Floquet growth rates λ_r, scaled by the beam amplitude parameter $\epsilon = 0.01$, as a function of the along-beam (ξ) wavenumber μ of the perturbations. Instability first arises around $\mu \approx 1$, and growth rates increase monotonically with μ until they eventually saturate to approximately 0.126 at $\mu = 20$. Figure 2(*b–d*) plots the time-frequency spectra of the Floquet modes corresponding to the growth rates shown in figure 2(*a*) at representative values of $\mu = 2.4$, 8.6 and 17. It should be noted that the different frequency components $\omega_p = \lambda_i + n\omega$ ($n = 0, \pm1, \pm2, \dots$) are discretized with spacing equal to ω in keeping with Floquet theory: the Floquet mode must be periodic with the same period as the basic state plus a constant offset term due to the imaginary part λ_i of the Floquet exponent. At low values of μ (e.g. $\mu = 2.4$), the frequency spectrum is dominated by two components at approximately $\pm f$ (figure 2*b*), matching the description of near-inertial PSI in KA17. However, as μ increases, the frequency spectrum broadens and $\pm f$ are no longer the dominant frequencies; for example, at $\mu = 17$, the dominant frequencies are now approximately $\pm 3f$ (figure 2*d*). As μ is further increased, the frequency spectrum continues to broaden and increasingly large frequencies dominate.

Figure 2(*e*) plots the spatial disturbances in the cross-beam (η) direction that correspond to the top four frequency components, in order of power, of the Floquet mode found at $\mu = 2.4$, which are the components at $\pm f$, followed by $\pm 3f$. All four spatial disturbances take the form of wavepackets with a well-defined carrier and locally confined envelope. Interestingly, the carrier wavenumbers γ of each of the four spatial disturbances, corresponding to the peak of the cross-beam (η) spatial Fourier spectrum computed from the Floquet analysis for a given μ, are all approximately equal, in this case to roughly -30. Figure 2(*f*) shows similar results for the Floquet mode found at $\mu = 8.6$, in which case $\gamma \approx -100$. In fact, all frequency components of a computed Floquet mode, and not just the top four, have approximately equal γ. Furthermore, figure 2(*b–d*) indicates that the frequency components of a given Floquet mode always appear in plus/minus pairs, while γ is always negative.

According to the above numerical results, the Floquet mode is a superposition of pairs of wavepackets, and each pair consists of waves that have approximately the same frequency and cross-beam wavenumber γ but travel in opposite directions. As the along-beam wavenumber μ is fixed, the carrier wavevector $\boldsymbol{k} = \mu\hat{\boldsymbol{e}}_\xi + \gamma\hat{\boldsymbol{e}}_\eta$ (figure 1*a*) of these wavepackets is approximately constant for all frequency components of the Floquet mode. Moreover, since $|\gamma| \gg |\mu| \gtrsim O(1)$, the perturbation has very fine scale relative to the primary beam, i.e. $|\boldsymbol{k}| \gg 1$, as assumed in KA17. According to the dispersion relation (2.3), for $\omega = 0.1$ and $f = \omega/2$, the beam inclination angle $\theta \approx 5^\circ$, so χ, the inclination angle of $\boldsymbol{k}$ to η, is approximately equal to θ; thus, $\boldsymbol{k}$, which is inclined to the vertical by $\phi = \theta - \chi$ (figure 1*a*), points nearly vertically. Therefore, only the subharmonic components at $\pm\omega/2$ of the Floquet mode approximately satisfy the dispersion relation (2.3) for the wavevector $\boldsymbol{k}$ and correspond essentially to freely propagating internal waves.

3.2. *Floquet stability versus near-inertial PSI*

The Floquet stability results for a small-amplitude beam ($\epsilon = 0.01$) with $\omega = 2f$ discussed above suggest that the instability dynamics assumed by KA17 for near-inertial PSI is valid only as long as the fine-scale perturbations have moderately large $|\boldsymbol{k}|$ (see figure 2*b*,*e*):

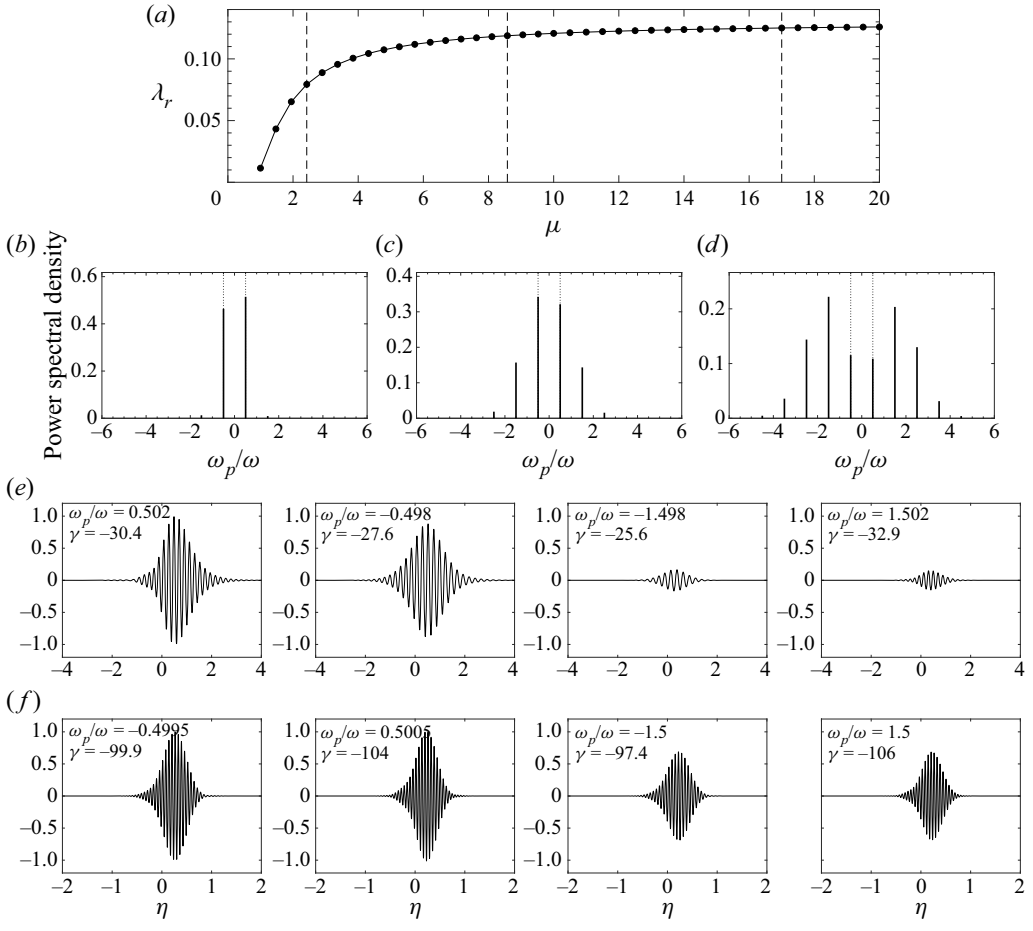

Figure 2. (*a*) Instability growth rates (scaled by the beam amplitude $\epsilon = 0.01$) predicted by the Floquet stability analysis as a function of the along-beam (ξ) wavenumber μ of the perturbations, for primary beam profile (3.1), beam frequency $\omega = 0.1$, Coriolis parameter $f = 0.05$ and inviscid flow conditions ($\nu = 0$). (*b*) Time frequency spectrum of the fastest growing Floquet mode for $\mu = 2.4$, indicated in panel (*a*) by a vertical dashed line. Vertical dotted lines indicate the frequencies $\pm f/\omega$. Here, the perturbation frequencies $\omega_p = \lambda_i + n\omega$, where λ_i is the imaginary part of the Floquet spectrum and $n = 0, \pm 1, \pm 2, \ldots$. Panels (*c*) and (*d*) are the same as panel (*b*) but for $\mu = 8.6$ and 17, respectively. (*e*) Spatial mode shapes for the top four frequencies, in order of power, of the frequency spectrum plotted in panel (*b*) for the Floquet mode at $\mu = 2.4$. From left to right, plots are shown in order of decreasing power. The spatial mode amplitudes have been normalized such that the mode corresponding to the top frequency component has maximum along-beam velocity equal to unity. The peak cross-beam (η) wavenumber γ of each mode is listed along with the frequency. Panel (*f*) is the same as panel (*e*) but for the top four frequencies, in order of power, of the frequency spectrum plotted in panel (*c*) for the Floquet mode at $\mu = 8.6$.

when μ and thereby $|\boldsymbol{k}|$ is increased while keeping ϵ fixed (e.g. figure 2*c*,*d*,*f*), the main hypothesis of PSI breaks down since the instability dynamics is no longer dominated by the subharmonic frequencies $\pm\omega/2$. These findings are consistent with the asymptotic scaling $|\boldsymbol{k}| = O(\epsilon^{-1/2})$ of KA17, which is clearly violated as $|\boldsymbol{k}| \to \infty$ for fixed ϵ. As a result of this restriction on $|\boldsymbol{k}|$, PSI does not capture the dominant inviscid instability (largest growth rate) which arises as $|\boldsymbol{k}| \to \infty$ (figure 2*a*). More importantly, however, quantitative comparison between the growth rates predicted by KA17 and our Floquet analysis revealed noticeable discrepancies even when PSI is valid (e.g. for $\mu = 2.4$ in figure 2*b*,*e*).

To understand and resolve these issues, we now turn to an asymptotic stability analysis of finite-width beams in the joint limit $\epsilon \ll 1$ and $|\boldsymbol{k}| \gg 1$, based on the full stability problem (2.5).

4. Small-amplitude limit of Floquet problem

4.1. *Preliminaries*

Since PSI is a two-dimensional instability, the following analysis assumes from the outset perturbations that only vary in the plane of the basic state (i.e. $m = 0$ in (2.4)). In this setting, rather than u and v, it is more convenient to introduce a stream function $\psi(\xi, \eta, t)$, in terms of which $u = \psi_\eta$ and $v = -\psi_\xi$. Thus, the incompressibility equation (2.1*a*) is automatically satisfied, and ψ, w and ρ are governed by the vorticity equation

$$\nabla^2\psi_t - \cos\theta\rho_\xi - \sin\theta\rho_\eta - f\sin\theta w_\xi + f\cos\theta w_\eta + J(\nabla^2\psi, \psi) - \nu\nabla^4\psi = 0, \quad (4.1)$$

along with the transverse momentum and continuity equations

$$w_t + f\sin\theta\psi_\xi - f\cos\theta\psi_\eta + J(w, \psi) - \nu\nabla^2 w = 0, \quad (4.2a)$$

$$\rho_t + \cos\theta\psi_\xi + \sin\theta\psi_\eta + J(\rho, \psi) = 0, \quad (4.2b)$$

where the Jacobian $J(a, b) = a_\xi b_\eta - a_\eta b_\xi$. Furthermore, in terms of the stream function, the basic state (2.2) that describes a uniform internal wave beam is replaced by

$$\psi_0 = \epsilon\, Q(\eta)\mathrm{e}^{-\mathrm{i}\omega t} + \text{c.c.}, \quad (4.3a)$$

$$w_0 = \epsilon\frac{\mathrm{i}f\cos\theta}{\omega}Q_\eta\mathrm{e}^{-\mathrm{i}\omega t} + \text{c.c.}, \quad (4.3b)$$

$$\rho_0 = -\epsilon\frac{\mathrm{i}\sin\theta}{\omega}Q_\eta\mathrm{e}^{-\mathrm{i}\omega t} + \text{c.c.}, \quad (4.3c)$$

where $Q(\eta)$ and the beam profile $U(\eta)$ in (2.2) are related by $\epsilon Q_\eta = U$, and ϵ is the amplitude parameter used earlier in (3.1). For convenience, here ϵ has been made explicit in (4.3) as the focus of this section centres around small-amplitude beams.

As in (2.4), we superimpose infinitesimal perturbations to this basic state in the form of normal modes

$$\psi = \psi_0 + \hat{\psi}(\eta, t)\mathrm{e}^{\mathrm{i}\mu\xi}, \quad (4.4)$$

with similar expressions for w and ρ, where μ is a real along-beam wavenumber parameter. Furthermore, in keeping with Floquet theory, $\hat{\psi}$ is expanded as a Fourier series in t with period $2\pi/\omega$, multiplied with an exponential term that contains the Floquet exponent λ,

$$\hat{\psi} = \mathrm{e}^{\lambda t}\sum_{n=-\infty}^{\infty}\hat{\psi}^{(n)}(\eta)\mathrm{e}^{\mathrm{i}n\omega t}, \quad (4.5)$$

with analogous expressions for $\hat{w}$ and $\hat{\rho}$. Inserting then (4.4) and (4.5) into (4.1) and (4.2) and linearizing leads to a set of infinite homogeneous equations for the perturbation amplitudes $\hat{\psi}^{(n)}$, $\hat{w}^{(n)}$ and $\hat{\rho}^{(n)}$, where $n = 0, \pm1, \pm2, \ldots$. This eigenvalue problem for λ, which determines stability, is of course equivalent to the one obtained earlier from (2.5) and can be tackled numerically by a similar procedure as in § 2.3.

Rather than proceeding numerically, however, here we seek an asymptotic approximation to this Floquet eigenvalue problem in the limit of a small-amplitude beam

($\epsilon \ll 1$) subject to fine-scale perturbations ($|\boldsymbol{k}| \gg 1$) in a nearly inviscid fluid ($\nu \ll 1$), the conditions under which PSI comes into play according to the numerical results in § 3.1. Specifically, as seen in figure 2(*e*), the spatial mode shapes $\hat{\psi}^{(n)}(\eta)$ in (4.5) take the form of wavepackets with a common carrier wavenumber γ in the cross-beam (η) direction. Therefore, we write

$$\left(\hat{\psi}^{(n)}, \hat{w}^{(n)}, \hat{\rho}^{(n)}\right) = \left(A^{(n)}(\eta), W^{(n)}(\eta), R^{(n)}(\eta)\right) \mathrm{e}^{\mathrm{i}\gamma\eta}. \tag{4.6}$$

Furthermore, we express the along- and cross-beam wavenumbers as

$$\mu = -k\sin\chi, \quad \gamma = k\cos\chi, \tag{4.7a,b}$$

where

$$k = \sqrt{\mu^2 + \gamma^2}, \quad \chi = \tan^{-1}(-\mu/\gamma) \tag{4.8a,b}$$

are the magnitude and inclination angle to the η direction, respectively, of the carrier wavevector $\boldsymbol{k} = \mu\hat{\boldsymbol{e}}_\xi + \gamma\hat{\boldsymbol{e}}_\eta$ (see figure 1*a*). Finally, to bring out the perturbation components with frequency $\omega/2$, without loss of generality, we take

$$\lambda \to \lambda - \mathrm{i}\frac{\omega}{2}. \tag{4.9}$$

As a result of the substitutions (4.6)–(4.9), the Floquet mode in (4.4) takes the form

$$\hat{\psi}(\eta, t)\mathrm{e}^{\mathrm{i}\mu\xi} = \mathrm{e}^{\lambda t}\mathrm{e}^{-\mathrm{i}\omega t/2}\exp(\mathrm{i}k(\eta\cos\chi - \xi\sin\chi))\sum_{n=-\infty}^{\infty} A^{(n)}(\eta)\mathrm{e}^{\mathrm{i}n\omega t}, \tag{4.10}$$

with similar expressions for $\hat{w}$ and $\hat{\rho}$. Furthermore, upon substituting (4.4) and (4.10) into (4.1) and (4.2), linearizing and collecting equal harmonics, it follows that the perturbation amplitudes $\tilde{A}^{(n)} = kA^{(n)}$, $W^{(n)}$ and $R^{(n)}$ ($n = 0, \pm1, \pm2, \dots$) satisfy the infinite equation system

$$\begin{aligned}
&(\lambda + \mathrm{i}(n-1/2)\omega)\,\mathbb{L}\tilde{A}^{(n)} + \mathrm{i}\left(\sin\phi R^{(n)} - f\cos\phi W^{(n)}\right) + \frac{1}{k}\left(\sin\theta R_\eta^{(n)} - f\cos\theta W_\eta^{(n)}\right)\\
&\quad -\mathrm{i}\sin\chi\left\{\epsilon k\left(Q_\eta\mathbb{L}\tilde{A}^{(n+1)} + Q_\eta^*\mathbb{L}\tilde{A}^{(n-1)}\right) + \frac{\epsilon}{k}\left(Q_{\eta\eta\eta}\tilde{A}^{(n+1)} + Q_{\eta\eta\eta}^*\tilde{A}^{(n-1)}\right)\right\}\\
&\quad +\nu k^2\mathbb{L}^2\tilde{A}^{(n)} = 0,
\end{aligned} \tag{4.11a}$$

$$\begin{aligned}
&(\lambda + \mathrm{i}(n-1/2)\omega)\,W^{(n)} - \mathrm{i}f\cos\phi\tilde{A}^{(n)} - \frac{f\cos\theta}{k}\tilde{A}_\eta^{(n)} + \nu k^2\mathbb{L}W^{(n)}\\
&-\mathrm{i}\sin\chi\left\{\epsilon k\left(Q_\eta W^{(n+1)} + Q_\eta^* W^{(n-1)}\right) - \frac{\mathrm{i}\epsilon f\cos\theta}{\omega}\left(Q_{\eta\eta}\tilde{A}^{(n+1)} - Q_{\eta\eta}^*\tilde{A}^{(n-1)}\right)\right\} = 0,
\end{aligned} \tag{4.11b}$$

$$\begin{aligned}
&(\lambda + \mathrm{i}(n-1/2)\omega)\,R^{(n)} + \mathrm{i}\sin\phi\,\tilde{A}^{(n)} + \frac{\sin\theta}{k}\tilde{A}_\eta^{(n)}\\
&-\mathrm{i}\sin\chi\left\{\epsilon k\left(Q_\eta R^{(n+1)} + Q_\eta^* R^{(n-1)}\right) + \frac{\mathrm{i}\epsilon\sin\theta}{\omega}\left(Q_{\eta\eta}\tilde{A}^{(n+1)} - Q_{\eta\eta}^*\tilde{A}^{(n-1)}\right)\right\} = 0,
\end{aligned} \tag{4.11c}$$

where

$$\mathbb{L} = 1 - \frac{2\mathrm{i}\cos\chi}{k}\frac{\mathrm{d}}{\mathrm{d}\eta} - \frac{1}{k^2}\frac{\mathrm{d}^2}{\mathrm{d}\eta^2}, \tag{4.12}$$

and $\phi = \theta - \chi$ is the inclination of $\boldsymbol{k}$ to the vertical (see figure 1*a*).

4.2. *PSI regime*

The eigenvalue problem (4.11), while equivalent to the one discussed in § 2.3, is a convenient starting point for examining the limit $\epsilon \ll 1$ and $k \gg 1$ appropriate for PSI. Specifically, for $k \gg 1$, the amplitudes $(\tilde{A}^{(n)}, W^{(n)}, R^{(n)})$ of the various frequency components that comprise the Floquet mode (4.10) correspond to the envelopes of the wavepackets found numerically in figure 2(*e*,*f*). According to (4.11), these amplitudes are coupled via the terms in the curly brackets which are $O(\epsilon k)$ to leading order. Therefore, when $\epsilon k = O(1)$, all frequency components may participate equally in the instability dynamics of a small-amplitude ($\epsilon \ll 1$) beam. This accounts for the broadening of the frequency spectrum of the instability at fixed ϵ as μ (and therefore k) is increased (figure 2*c*,*d*).

By contrast, when

$$\epsilon k \ll 1 \tag{4.13}$$

in (4.11), the amplitudes of the frequency components of the Floquet mode are weakly coupled. In this instance, it is possible to asymptotically truncate the Fourier series in (4.10) so that a finite number of frequency components dominate the instability dynamics, as is the case in PSI. Thus, we now turn our attention to the joint limit

$$\epsilon \ll 1, \quad k \gg 1, \tag{4.14a,b}$$

under the condition (4.13) and, as seen in figure 2(*b*), we assume that the frequencies $-\omega/2$ and $\omega/2$, which correspond to $n = 0$ and $n = 1$ in (4.10), dominate the instability. Then, from (4.11), the rest of the harmonics are less important

$$\left(\tilde{A}^{(n)}, W^{(n)}, R^{(n)}\right) = \begin{cases} O\left((\epsilon k)^{n-1}\right)\tilde{A}^{(1)}, & (n \geq 2), \\ O\left((\epsilon k)^{|n|}\right)\tilde{A}^{(0)}, & (n \leq -1). \end{cases} \tag{4.15}$$

Furthermore, after eliminating $W^{(0)}$, $W^{(1)}$, $R^{(0)}$ and $R^{(1)}$, and making use of (4.13)–(4.15), the equations for the dominant $n = 0$ and $n = 1$ components of (4.11) can be approximated as

$$\begin{aligned} &\mathrm{i}\Omega\tilde{A}^{(0)} + \omega\left(\lambda + \nu k^2\beta\right)\tilde{A}^{(0)} + \frac{\omega c}{k}\tilde{A}^{(0)}_{\eta} - \mathrm{i}\frac{3\omega^2}{4k^2}\tilde{A}^{(0)}_{\eta\eta} \\ &\quad + \epsilon k\mathrm{i}\sin\chi\left\{\Omega\frac{2}{\omega}Q_{\eta}\tilde{A}^{(1)} - Q^{*}_{\eta}\left(\sin\phi\, R^{(-1)} - f\cos\phi W^{(-1)} + \frac{\omega}{2}\tilde{A}^{(-1)}\right)\right\} \\ &\quad - \epsilon^2k^2\mathrm{i}\sin^2\chi\left(1 + \frac{4\Omega}{\omega^2}\right)|Q_{\eta}|^2\tilde{A}^{(0)} + \epsilon\frac{\sin\chi}{\omega}\left\{3\delta Q_{\eta\eta}\tilde{A}^{(1)} + 2\omega c Q_{\eta}\tilde{A}^{(1)}_{\eta}\right\} \\ &\quad = O\left(\frac{\epsilon}{k}, \epsilon^2\right), \end{aligned} \tag{4.16a}$$

$$\begin{aligned} &-\mathrm{i}\Omega\tilde{A}^{(1)} + \omega\left(\lambda + \nu k^2\beta\right)\tilde{A}^{(1)} - \frac{\omega c}{k}\tilde{A}^{(1)}_{\eta} + \mathrm{i}\frac{3\omega^2}{4k^2}\tilde{A}^{(1)}_{\eta\eta} \\ &\quad + \epsilon k\mathrm{i}\sin\chi\left\{\Omega\frac{2}{\omega}Q^{*}_{\eta}\tilde{A}^{(0)} + Q_{\eta}\left(\sin\phi R^{(2)} - f\cos\phi W^{(2)} - \frac{\omega}{2}\tilde{A}^{(2)}\right)\right\} \\ &\quad + \epsilon^2k^2\mathrm{i}\sin^2\chi\left(1 + \frac{4\Omega}{\omega^2}\right)|Q_{\eta}|^2\tilde{A}^{(1)} + \epsilon\frac{\sin\chi}{\omega}\left\{3\delta Q^{*}_{\eta\eta}\tilde{A}^{(0)} + 2\omega c Q^{*}_{\eta}\tilde{A}^{(0)}_{\eta}\right\} \\ &\quad = O\left(\frac{\epsilon}{k}, \epsilon^2 k\right), \end{aligned} \tag{4.16b}$$

where

$$\Omega = \sin^2\phi + f^2\cos^2\phi - \frac{\omega^2}{4}, \tag{4.17a}$$

$$\beta = \frac{1}{2}\left(1 + \frac{4f^2\cos^2\phi}{\omega^2}\right), \quad \delta = \sin\phi\sin\theta + f^2\cos\phi\cos\theta, \tag{4.17b}$$

$$c = \frac{2}{\omega}\left(\delta - \frac{\omega^2}{4}\cos\chi\right). \tag{4.17c}$$

Here, in deriving (4.16), it is assumed that

$$\lambda \sim \nu k^2 \ll 1, \tag{4.18}$$

anticipating that in the weak-coupling limit (4.13) instability is weak, and including only the leading-order effects of viscosity.

The $O(1)$ terms in (4.16) drop out as the carrier wavevector $\boldsymbol{k}$ has to adhere to the dispersion relation (2.3) for the dominant frequencies $\pm\omega/2$, so $\Omega = 0$ in (4.17*a*). Furthermore, from (4.11), the amplitudes of the frequency components $\pm 3\omega/2$, to leading order, are given as

$$\tilde{A}^{(-1)} = -\epsilon k\frac{\sin\chi}{\omega}Q_\eta\tilde{A}^{(0)}, \quad \tilde{A}^{(2)} = \epsilon k\frac{\sin\chi}{\omega}Q_\eta^*\tilde{A}^{(1)}, \tag{4.19a}$$

$$\left(R^{(-1)}, R^{(2)}\right) = \frac{2\sin\phi}{\omega}\left(\tilde{A}^{(-1)}, -\tilde{A}^{(2)}\right), \tag{4.19b}$$

$$\left(W^{(-1)}, W^{(2)}\right) = \frac{2f\cos\phi}{\omega}\left(-\tilde{A}^{(-1)}, \tilde{A}^{(2)}\right). \tag{4.19c}$$

As a result, inserting (4.19) into (4.16), we find that all interaction terms at $O(\epsilon k)$ and $O(\epsilon^2 k^2)$ vanish, leaving the following closed system for $\tilde{A}^{(0)}$ and $\tilde{A}^{(1)}$:

$$\left(\lambda + \nu k^2\beta\right)\tilde{A}^{(0)} + \frac{c}{k}\tilde{A}^{(0)}_\eta - \mathrm{i}\frac{3\omega}{4k^2}\tilde{A}^{(0)}_{\eta\eta} + \epsilon\frac{\sin\chi}{\omega^2}\left\{3\delta Q_{\eta\eta}\tilde{A}^{(1)} + 2\omega c\, Q_\eta\tilde{A}^{(1)}_\eta\right\} = O\left(\frac{\epsilon}{k}, \epsilon^2 k\right), \tag{4.20a}$$

$$\left(\lambda + \nu k^2\beta\right)\tilde{A}^{(1)} - \frac{c}{k}\tilde{A}^{(1)}_\eta + \mathrm{i}\frac{3\omega}{4k^2}\tilde{A}^{(1)}_{\eta\eta} + \epsilon\frac{\sin\chi}{\omega^2}\left\{3\delta Q^*_{\eta\eta}\tilde{A}^{(0)} + 2\omega c\, Q^*_\eta\tilde{A}^{(0)}_\eta\right\} = O\left(\frac{\epsilon}{k}, \epsilon^2 k\right). \tag{4.20b}$$

These two coupled equations (along with the boundary conditions $\tilde{A}^{(0)}, \tilde{A}^{(1)} \to 0$ as $\eta \to \pm\infty$) define an eigenvalue problem for λ that governs the stability of small-amplitude finite-width beams under the conditions (4.13), (4.14*a*,*b*) and (4.18), appropriate to PSI. This reduced system captures the effects of the group velocity and dispersion of the subharmonic perturbation wavepackets, as well as the leading-order effects of the interaction of these wavepackets with the underlying beam, and weak viscous dissipation.

In view of (4.13) and (4.14*a*,*b*), the $O(1/k)$ group velocity effect in (4.20) always dominates the $O(\epsilon)$ interaction of the perturbation with the beam, the only term that can cause instability. On these grounds KA14 argued that a small-amplitude finite-width beam cannot suffer PSI in general. Furthermore, from this scaling argument follow two notable

special cases: (i) near-inertial PSI (considered in KA17 and revisited in § 5 below), where the group velocity c in (4.17*c*) happens to be small; and (ii) PSI of a beam with nearly monochromatic profile (considered in KA14 and revisited in § 6 below), where the triad interaction of the subharmonic perturbations with the beam is finely tuned and can lead to instability.

Finally, turning to the full Floquet stability eigenvalue problem (4.11), a small-amplitude ($\epsilon \ll 1$) beam with general locally confined profile could be unstable to fine-scale ($k \gg 1$) perturbations with $\epsilon k = O(1)$. In this regime, while the Floquet mode frequency spectrum broadens, figure 2(*a*) suggests that the instability growth rate remains $O(\epsilon)$. Thus, as explained in § 7, it becomes possible to set up a separate asymptotic model for $\epsilon \ll 1$, $k \gg 1$ and $\epsilon k = O(1)$, which reveals a new, broadband instability of small-amplitude beams.

5. Near-inertial PSI

5.1. *Reduced eigenvalue problem*

We now revisit near-inertial PSI in the light of the small-amplitude theory of § 4 and the numerical Floquet analysis of § 3. To allow for slight deviations from the critical frequency $\omega = 2f$, we write

$$\omega = 2f + \sigma, \tag{5.1}$$

where $|\sigma| \ll 1$ is a detuning parameter.

Here, it is important to note that when $\omega < 2f$ (i.e. $\sigma < 0$), perturbations at half this frequency are subinertial ($\omega/2 < f$) so in (4.16) the dispersion relation $\Omega = 0$ cannot be satisfied by a real wavevector $\boldsymbol{k}$. However, it is still possible to allow for slightly subinertial subharmonic perturbations in our asymptotic approach by inserting (5.1) into (4.11) from the onset. This results in two additional terms, $\omega\sigma\tilde{A}^{(0)}/2$ in (4.16*a*) and $\omega\sigma\tilde{A}^{(1)}/2$ in (4.16*b*), which incorporate the effect of small detuning. Since $\omega/2 = f$ to leading order, with the inclusion of these additional terms it is sufficient now to take, without loss of generality, $\phi = 0$ (i.e. $\boldsymbol{k}$ points vertically) so that $\Omega = 0$ and the $O(1)$ terms in (4.16) again drop out. Furthermore, for this choice of ϕ, the group velocity terms in (4.20) can be neglected in view of (4.17). The remaining terms of (4.20) – which represent the effects of wavepacket dispersion, coupling to the underlying beam, viscous dissipation and departure from the critical frequency – may then be formally balanced by the scalings

$$\lambda \to \epsilon\lambda, \quad \nu = \alpha\epsilon^2, \quad k = \frac{\kappa}{\epsilon^{1/2}}, \quad \sigma = \epsilon f\hat{\sigma}, \tag{5.2a–d}$$

consistent with (4.14*a*,*b*) and (4.18). In this 'distinguished limit', making also use of (4.17), the eigenvalue problem (4.20) reduces to

$$\left(\frac{\hat{\lambda}}{\omega/2} - \mathrm{i}\frac{\hat{\sigma}}{2}\right)\tilde{A}^{(0)} - \mathrm{i}\frac{3}{2\kappa^2}\tilde{A}^{(0)}_{\eta\eta} + \frac{3\sin 2\theta}{4\omega}Q_{\eta\eta}\tilde{A}^{(1)} = 0, \tag{5.3a}$$

$$\left(\frac{\hat{\lambda}}{\omega/2} + \mathrm{i}\frac{\hat{\sigma}}{2}\right)\tilde{A}^{(1)} + \mathrm{i}\frac{3}{2\kappa^2}\tilde{A}^{(1)}_{\eta\eta} + \frac{3\sin 2\theta}{4\omega}Q^*_{\eta\eta}\tilde{A}^{(0)} = 0, \tag{5.3b}$$

where

$$\hat{\lambda} = \lambda + \alpha\kappa^2. \tag{5.4}$$

For a given beam profile Q, the eigenvalues $\hat{\lambda}$ depend on the parameters ω, $\hat{\sigma}$ and κ, and instability arises when $\hat{\lambda} > \alpha\kappa^2$. Accordingly, $\hat{\lambda}$ can be interpreted as the inviscid growth rate.

The stability eigenvalue problem (5.3) is similar, but not entirely equivalent, to the one obtained in KA17 for near-inertial PSI. Specifically, the present asymptotic analysis, which is based on the full Floquet stability problem (4.11), reveals the importance of the $\pm 3\omega/2$ frequency components (4.19) in the PSI dynamics: including these disturbances cancels out the terms proportional to $|Q_\eta|^2$ in (4.16), which thus do not appear in the final stability equations (5.3). In contrast, KA17 focuses solely on the $\pm\omega/2$ frequency components so these 'nonlinear refraction' terms erroneously are present in the stability eigenvalue problem of KA17 (cf. their (28)). This resolves the discrepancy noted in § 3.2 between KA17 and the numerical Floquet analysis: the predictions of the eigenvalue problem (5.3) are in excellent agreement with Floquet numerical results for near-inertial PSI, as discussed below. Furthermore, it should be noted that KA17 assumes $\omega \geq 2f$, whereas our analysis permits the detuning parameter to be of either sign, encompassing both superinertial and subinertial perturbations. The present, more general, treatment reduces to that of KA17 by setting $\hat{\sigma} = \sigma_{KA}^2(1 - f^2)/f^2$ and $(\tilde{A}^{(0)}, \tilde{A}^{(1)}) \to (\tilde{A}^{(0)}, \tilde{A}^{(1)}) \exp(\mathrm{i}\kappa\sigma_{KA}\eta/\sin\theta)$, where σ_{KA} is the detuning parameter used in KA17.

5.2. *Instability growth rates*

We now compare the predictions of (5.3) with those of the numerical Floquet analysis. To this end, Q in (5.3) is chosen as

$$Q(\eta) = \frac{1}{\sqrt{8\pi}} \int_0^\infty \mathrm{e}^{-l^2/8} \mathrm{e}^{\mathrm{i}l\eta} \mathrm{d}l, \tag{5.5}$$

which corresponds to the same beam profile (3.1) used earlier (and also matches the profile used in KA17). Furthermore, as in § 3, $\omega = 0.1$ and all reported growth rates λ_r will be in the scaled time $T = \epsilon t$ consistent with (5.2*a–d*). Numerically, the eigenvalue problem (5.3) was discretized in η using eighth-order centred differences and the resulting matrix eigenvalue problem was solved using standard numerical eigenvalue algorithms in MATLAB for the eigenvalue $\hat{\lambda}$. The computational domain was varied between $\eta \in [-5, 5]$ and $[-100, 100]$, depending on the choices of κ and $\hat{\sigma}$, with a typical grid size of 2000 points.

Figure 3 compares the instability growth rates λ_r predicted by the numerical Floquet analysis and the near-inertial PSI theory (5.3) under various flow conditions. Specifically, the PSI growth rates are plotted as a function of the perturbation wavenumber $\kappa > 0$ for viscosity parameter $\alpha = 0$ and 10^{-3}, and detuning parameter $\hat{\sigma} = -4, -2, 0, 4, 10$ and 20. The corresponding Floquet growth rates are shown for beam amplitude $\epsilon = 0.002$, with κ computed using (4.8*a*,*b*) and (5.2*a–d*), where γ is taken to be the average of the carrier wavenumbers (in η) of the two subharmonic frequency components. For this ϵ, the largest detuning parameter chosen here, $\hat{\sigma} = 20$, corresponds to $\omega/f = 2.04$, which translates to a frequency detuning of approximately 2 %. A discussion of results for varying ϵ is presented later (see figure 5).

Overall, we observe excellent quantitative agreement between the fully numerical and the asymptotic instability growth rates. In the inviscid case ($\alpha = 0$) shown in figure 3(*a*,*c*), $\lambda_r = \hat{\lambda}_r$ saturates to an approximately constant value for large κ that depends on the detuning $\hat{\sigma}$. As $|\hat{\sigma}|$ increases, i.e. as $\omega/2$ moves away from f, this limiting growth rate is diminished, a stabilizing effect that is stronger for $\hat{\sigma} < 0$ (i.e. $\omega/2 < f$). In this

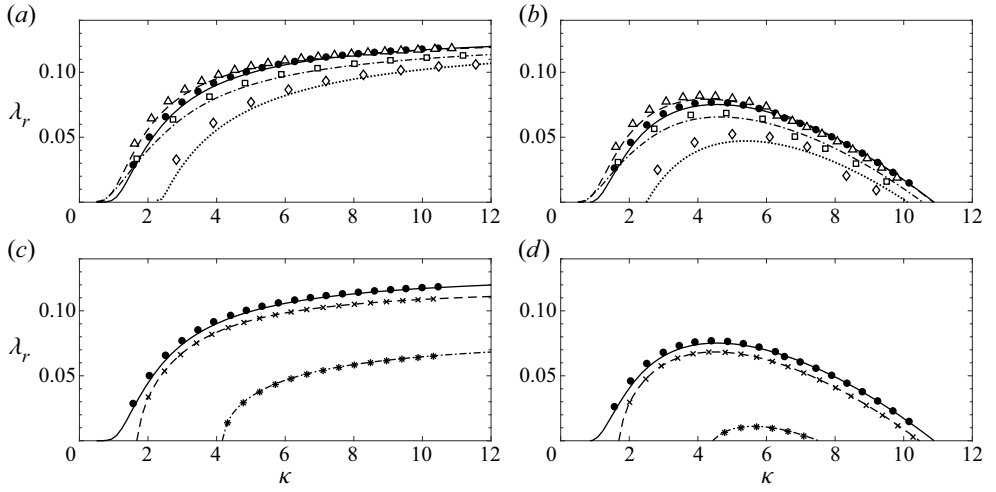

Figure 3. Comparison of predicted instability growth rates (in terms of the scaled time $T = \epsilon t$) as a function of the scaled perturbation wavenumber κ between the near-inertial PSI theory (using beam profile (5.5)) and the Floquet analysis (using beam profile (3.1) with beam amplitude $\epsilon = 0.002$) for primary beam frequency $\omega = 0.1$. Results are shown for viscous parameter (*a*,*c*) $\alpha = 0$ corresponding to inviscid flow and (*b*,*d*) $\alpha = 10^{-3}$. Panels (*a*,*b*) show results for detuning parameter $\hat{\sigma} = 0$ (•, solid line), $\hat{\sigma} = 4$ (△, dashed line), $\hat{\sigma} = 10$ (□, dashed-dotted line) and $\hat{\sigma} = 20$ (◇, dotted line). Panels (*c*,*d*) show results for $\hat{\sigma} = 0$ (•, solid line), $\hat{\sigma} = -2$ (×, dashed line), $\hat{\sigma} = -4$ (∗, dashed-dotted line). In all plots, shapes correspond to the Floquet growth rate while lines correspond to the near-inertial PSI growth rate.

instance, the computed PSI growth rates have zero imaginary part ($\lambda_i = 0$) so in view of (4.10), subinertial subharmonic perturbations have frequency exactly equal to $\omega/2$, also in agreement with the numerical Floquet analysis. For finite viscosity, as illustrated in figure 3(*b*,*d*) for $\alpha = 10^{-3}$, instability is confined to a finite range of κ. This is to be expected based on the near-inertial PSI theory: as κ is increased, the quadratic $\alpha\kappa^2$ will eventually exceed $\hat{\lambda}_r$, the inviscid growth rate, which is approximately constant at large κ. Here, it should be noted that $\alpha = 10^{-3}$ with $\epsilon = 0.002$ sets the inverse Reynolds number $\nu = O(10^{-9})$ and corresponds to nearly inviscid conditions, as would be found in oceans.

Figure 4 plots the maximum instability growth rate, taken over κ, as a function of the detuning $-6 \leq \hat{\sigma} \leq 20$. Again, there is excellent agreement between the near-inertial PSI theory and the Floquet analysis. As illustrated in figure 4, instability is completely suppressed regardless of viscous dissipation when $\omega/2$ is sufficiently subinertial ($\hat{\sigma} \lesssim -5$). For inviscid flow conditions (figure 4*a*), the maximum instability growth rate, which is found as $\kappa \to \infty$ for a given detuning $\hat{\sigma}$, shows very weak dependence on $\hat{\sigma}$ for $\hat{\sigma} \geq 0$. Under viscous flow conditions ($\alpha = 10^{-3}$), shown in figure 4(*b*), the maximum growth rate decreases for large $\hat{\sigma}$, indicating that instability is weakened far enough from near-inertial conditions. Interestingly, though, for finite viscosity, instability is strongest at small but finite $\hat{\sigma} > 0$, rather than exactly at the critical $\omega = 2f$ ($\hat{\sigma} = 0$). This is due to the behaviour of the growth rates near the onset of instability: as illustrated in figure 3(*a*,*b*), the growth rates for $\hat{\sigma} = 4$ arise at slightly lower κ and have larger values in the range $1 \lesssim \kappa \lesssim 5$ than the growth rates for $\hat{\sigma} = 0$.

Finally, figure 5 compares the Floquet and PSI growth rates under inviscid flow conditions ($\alpha = 0$) at three different values of the detuning $\hat{\sigma} = -4, 0$ and 20 for the beam amplitudes $\epsilon = 0.002, 0.01, 0.05$ and 0.1. For $\hat{\sigma} = 0$, the Floquet growth rates for the larger $\epsilon = 0.2$ are also shown. As expected, the best agreement between the PSI theory

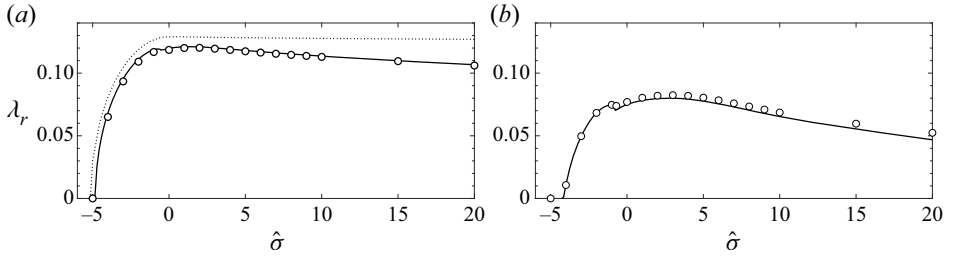

Figure 4. Maximum instability growth rate as function of detuning $-6 \leq \hat{\sigma} \leq 20$ for the same primary beam as in figure 3. (*a*) Inviscid flow conditions ($\alpha = 0$). In this case, since the maximum growth rate for a given $\hat{\sigma}$ occurs as $\kappa \to \infty$ (see figure 3*a*,*c*), results are presented for the near-inertial PSI growth rate at $\kappa = 12$ (solid line) and $\kappa = 100$ (dotted line). Floquet results (○) are shown at $\kappa \approx 12$. (*b*) Viscous flow conditions ($\alpha = 10^{-3}$). In this case, since the maximum growth rate is achieved at finite κ (see § 5.2), plotted growth rates correspond to the maximum over all κ. Solid line is the near-inertial PSI growth rate, while (○) is the Floquet growth rate.

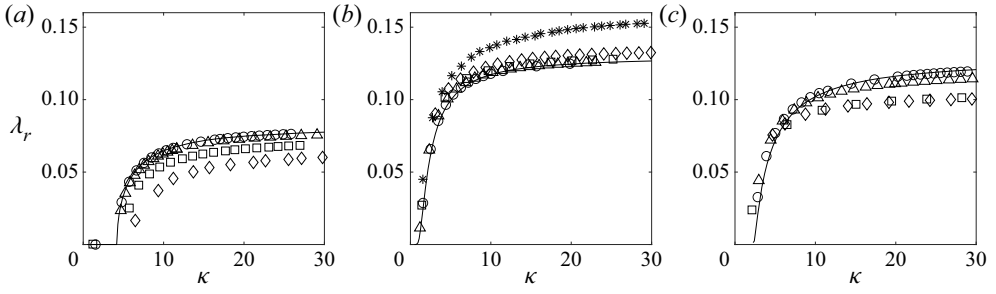

Figure 5. Inviscid instability growth rate as a function of the scaled perturbation wavenumber κ predicted by the Floquet analysis for beam amplitude $\epsilon = 0.002$ (○), 0.01 (△), 0.05 (□), 0.1 (◇). The same primary beam profile and frequency as in figures 3 and 4 are used here. Plots correspond to detuning parameter $\hat{\sigma} = -4$ (*a*), $\hat{\sigma} = 0$ (*b*) and $\hat{\sigma} = 20$ (*c*). The results for $\hat{\sigma} = 0$ in panel (*b*) include Floquet growth rates for $\epsilon = 0.2$ (∗). Solid lines correspond to the near-inertial PSI growth rate.

and the Floquet analysis is found when the assumptions $\epsilon \ll 1$, $\epsilon k \ll 1$ ($\kappa \lesssim \epsilon^{-1/2}$) and $|\hat{\sigma}| = O(1)$ made in the PSI theory are well satisfied. It should be noted that typical values for oceanic internal waves, with characteristic velocity $U_* \approx 0.1$ m s^{-1}, characteristic beam width $L_* \approx 500$ m, and buoyancy frequency $N_* \approx 2 \times 10^{-3}$ s^{-1} (see e.g. Gerkema, Lam & Maas 2004), result in the dimensionless amplitude $\epsilon \approx 0.1$.

5.3. *Instability dynamics*

The results presented above indicate that the instability growth rates predicted by the numerical Floquet analysis agree well with the near-inertial PSI theory. However, as illustrated in figure 2 and discussed in § 4.2, the main assumption of PSI theory, namely that the frequency components at $\pm\omega/2$ dominate, eventually breaks down as κ is increased with ϵ fixed. More precisely, the PSI theory fails when $\kappa = O(\epsilon^{-1/2})$, in keeping with (4.13) and (5.2*a–d*), and unstable Floquet modes contain broadband frequency spectra.

To confirm these theoretical predictions, we return to the instability growth rate curve in figure 2(*a*). When plotted in terms of the scaled wavenumber magnitude κ rather than the along-beam wavenumber μ, this curve corresponds to the growth rate curve in figure 5(*b*) for $\hat{\sigma} = 0$ and $\epsilon = 0.01$ and is nearly indistinguishable from the predictions of the

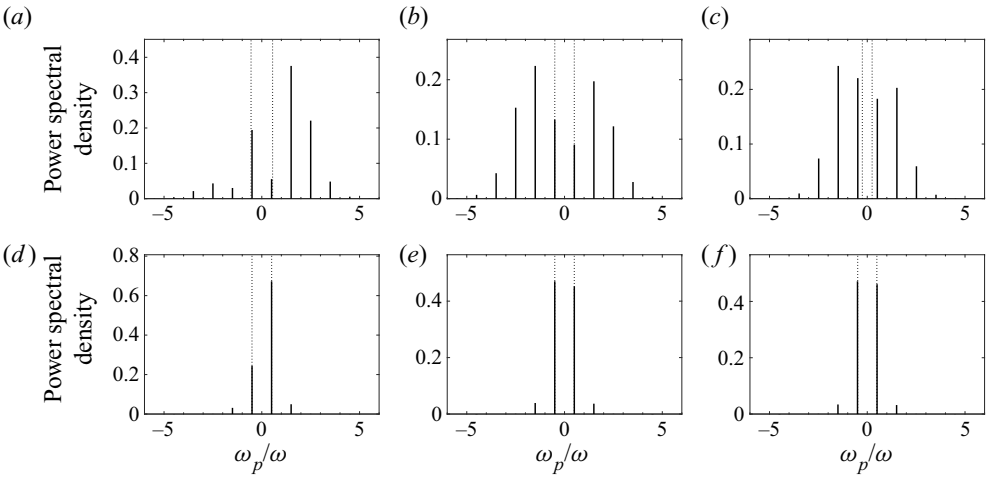

Figure 6. Time-frequency spectra of the fastest-growing Floquet mode found at scaled perturbation wavenumber $\kappa = 10$ for the same primary beam profile and frequency used throughout § 5. Panels (*a–c*) show modes for beam amplitude $\epsilon = 0.05$ while panels (*d–f*) show modes for $\epsilon = 0.002$. Panels (*a*,*d*), (*b*,*e*) and (*c*,*f*) correspond to detuning parameter $\hat{\sigma} = -4$, 0 and 20, respectively. The vertical dotted lines indicate the frequencies $\pm f/\omega$.

PSI theory. However, despite this agreement, the time-frequency spectra in figure 2(*b–d*), which correspond to $\kappa \approx 3$, 10 and 20, respectively, indicate that the instability dynamics for $\kappa \gtrsim 10$ does not resemble PSI at all, consistent with the estimate $\kappa \approx \epsilon^{-1/2} = 10$ for the breakdown of the PSI assumption. Furthermore, figure 6 compares the time-frequency spectra of the most unstable inviscid Floquet modes at $\kappa = 10$ for beam amplitudes $\epsilon = 0.002$ and 0.05 and detuning $\hat{\sigma} = -4$, 0 and 20. Since these Floquet modes exactly correspond to the growth rates shown in figure 5 at $\kappa = 10$, the Floquet growth rate is in excellent agreement with the PSI theory for both beam amplitudes. However, for the larger amplitude $\epsilon = 0.05$ (figure 6*a–c*), the frequency spectra indicate that the instability dynamics does not correspond to PSI, consistent with $\epsilon k \approx 2$ not being small.

In summary, when $\epsilon k \ll 1$ the near-inertial PSI theory is in excellent agreement with the numerical Floquet analysis. When ϵk is not small, instability is not dominated by the subharmonic frequencies at $\pm\omega/2$, consistent with the conclusion reached in § 4.2. Remarkably, however, PSI theory, even though it is not formally valid in this regime, still provides reliable predictions for the instability growth rate. A similar observation was made by Sonmor & Klaassen (1997) for the instability of a sinusoidal wave (see their § 4*a*). The reason for the wider than expected validity of PSI theory is discussed in § 7.

6. PSI of nearly monochromatic beams

6.1. *Reduced eigenvalue problem*

Aside from near-inertial conditions, PSI is also possible for small-amplitude locally confined beams with a nearly monochromatic profile, as pointed out in KA14. This study assumed no background rotation ($f = 0$), so the beam frequency obeys $\omega = \sin\theta$ according to (2.3), and omitted the contribution of the $\pm 3\omega/2$ frequency components to PSI dynamics. However, unlike near-inertial PSI, these frequencies do not affect the stability eigenvalue problem derived in KA14.

Here, we compare the predictions of PSI theory with those of Floquet stability analysis for a nearly monochromatic beam under the conditions assumed in KA14. To this end, rather than quoting KA14, it is more economical to derive the PSI eigenvalue problem directly from the small-amplitude limit of the Floquet stability problem discussed in § 4. Specifically, we return to (4.20) and consider a beam with profile

$$Q(\eta) = q(H)\mathrm{e}^{\mathrm{i}\eta}, \quad H = \hat{\epsilon}\eta. \tag{6.1a,b}$$

Here, H is a stretched envelope coordinate and $\hat{\epsilon} \ll 1$ is a small parameter (made precise in (6.4*a–d*) below) that controls the width of the slowly varying envelope $q(H)$ relative to the characteristic length scale $L_* = \Lambda_*/2\pi$, where Λ_* is the carrier wavelength of the primary wave beam. It should be noted that under the present conditions, the dispersion relation $\Omega = 0$ in (4.16) is exactly satisfied by choosing $\sin\phi = \omega/2$.

In view of (6.1*a*,*b*), the perturbation amplitudes $\tilde{A}^{(0,1)}$ take the form

$$\tilde{A}^{(0)}(\eta) \to \tilde{A}^{(0)}(H)\mathrm{e}^{\mathrm{i}(\eta/2)}, \quad \tilde{A}^{(1)}(\eta) \to \tilde{A}^{(1)}(H)\mathrm{e}^{-\mathrm{i}(\eta/2)}, \tag{6.2a,b}$$

and inserting (6.1*a*,*b*) and (6.2*a*,*b*) into the stability equations (4.20), we find at leading order

$$\left(\lambda + \frac{1}{2}\nu k^2 + \mathrm{i}\frac{c}{2k} + \mathrm{i}\frac{3\omega}{16k^2}\right)\tilde{A}^{(0)} + \hat{\epsilon}\frac{c}{k}\tilde{A}_H^{(0)} - \epsilon\sin\chi\cos^2\left(\frac{\chi}{2}\right)q\tilde{A}^{(1)} = 0, \tag{6.3a}$$

$$\left(\lambda + \frac{1}{2}\nu k^2 + \mathrm{i}\frac{c}{2k} - \mathrm{i}\frac{3\omega}{16k^2}\right)\tilde{A}^{(1)} - \hat{\epsilon}\frac{c}{k}\tilde{A}_H^{(1)} - \epsilon\sin\chi\cos^2\left(\frac{\chi}{2}\right)q^*\tilde{A}^{(0)} = 0. \tag{6.3b}$$

The various terms in (6.3) may then be formally balanced in a similar fashion to the near-inertial PSI analysis (cf. (5.2*a–d*)), by the scalings

$$\lambda \to \epsilon\lambda, \quad \nu = 2\alpha\epsilon^2, \quad k = \frac{\kappa}{\epsilon^{1/2}}, \quad \hat{\epsilon} = \frac{\epsilon^{1/2}}{D}. \tag{6.4a–d}$$

Here,

$$D = 2\pi N\epsilon^{1/2} = O(1) \tag{6.5}$$

is a scaled width of the beam envelope in terms of N, the number of carrier wavelengths contained within the beam. Inserting (6.4*a–d*) into (6.3) and making the substitutions $\tilde{A}^{(0,1)} \to \tilde{A}^{(0,1)}\exp[-3\mathrm{i}\omega H/(16c\hat{\epsilon}k)]$ and $\lambda \to \lambda - \mathrm{i}c/(2k)$, which do not affect stability, we find that the PSI of nearly monochromatic beams is governed by

$$\hat{\lambda}\tilde{A}^{(0)} + \frac{c}{D\kappa}\tilde{A}_H^{(0)} - \sin\chi\cos^2\left(\frac{\chi}{2}\right)q\tilde{A}^{(1)} = 0, \tag{6.6a}$$

$$\hat{\lambda}\tilde{A}^{(1)} - \frac{c}{D\kappa}\tilde{A}_H^{(1)} - \sin\chi\cos^2\left(\frac{\chi}{2}\right)q^*\tilde{A}^{(0)} = 0, \tag{6.6b}$$

where

$$\hat{\lambda} = \lambda + \alpha\kappa^2. \tag{6.7}$$

As noted earlier, the final stability eigenvalue problem (6.6) is identical to that found by KA14 (see their (4.10)), as the frequency components at $\pm 3\omega/2$, omitted in KA14, ultimately do not play a role in the PSI stability analysis of nearly monochromatic beams.

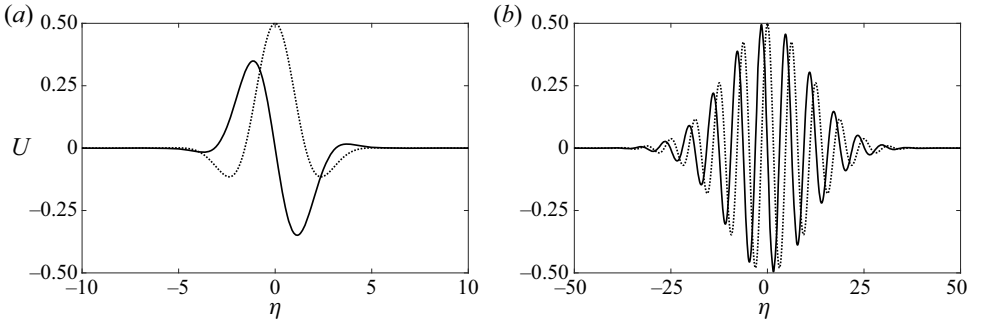

Figure 7. Beam profile (6.9) for non-dimensional amplitude $\epsilon = 1$ and (*a*) $N = 1$ and (*b*) $N = 7$, where N corresponds to the number of carrier wavelengths contained within the beam width. Solid lines indicate the real part, while dotted lines indicate the imaginary part.

6.2. *Comparison with Floquet analysis*

We now compare the Floquet stability analysis of a nearly monochromatic beam with the predictions of the PSI theory (6.6). Specifically, we chose the Gaussian envelope profile

$$q(H) = \tfrac{1}{2}\exp(-8H^2). \tag{6.8}$$

Combined with (6.1*a*,*b*), (6.4*a*–*d*) and (6.5), (6.8) corresponds to the overall beam profile

$$U(\eta) = \mathrm{i}\frac{\epsilon}{2}\exp\left(-\frac{2\eta^2}{\pi^2 N^2}\right)\exp(\mathrm{i}\eta) \tag{6.9}$$

in (2.2) for the Floquet analysis. Figure 7 plots the beam profile (6.9) for $N = 1$ and 7. We recall that, according to (6.5), $N = O(\epsilon^{-1/2})$ in the PSI theory. Numerically, the eigenvalue problem (6.6) was discretized in the domain $H \in [-5, 5]$ using eighth-order centred differences with a grid size of 500 points, and the resulting matrix eigenvalue problem was solved using standard numerical eigenvalue algorithms in MATLAB for the eigenvalue $\hat{\lambda}$. The discussion below will focus on the beam inclination angle $\theta = 45^\circ$ (which is tied to the beam frequency via the dispersion relation $\omega = \sin\theta$) and inverse Reynolds number $\nu = 10^{-5}$. The effect of varying θ is discussed in Fan (2020, § 3.6.3).

Figure 8(*a*) plots the maximum instability growth rates (taken over κ and given in terms of the slow time $T = \epsilon t$) predicted by the PSI theory and the Floquet analysis as a function of N, the number of carrier wavelengths of the beam profile, for various values of $0.025 \leq \epsilon \leq 0.4$. As expected, in the limit of $N \to \infty$, the PSI growth rates converge onto the sinusoidal wave growth rate. Furthermore, the Floquet growth rates show excellent agreement with the PSI theory for all $\epsilon \leq 0.4$ and $N \geq 2$, even though in these parameter ranges neither the assumption of small amplitude (i.e. $\epsilon \ll 1$) nor the assumption of scale separation between the carrier and the envelope (i.e. $N \gg 1$) are necessarily well satisfied.

Furthermore, based on PSI theory, KA14 proposed a lower bound on N, the number of carrier wavelengths contained in the beam envelope, for PSI to arise (see their (5.14)). By rearranging their expression for this lower bound, which depends on various parameters including the inverse Reynolds number ν and beam amplitude ϵ, we deduce a minimum amplitude threshold for instability, at fixed N,

$$\epsilon_c = \left(\frac{1}{2\mathbb{C}_c}\right)^{1/3}\frac{c^{2/3}}{\Gamma}\frac{\nu^{1/3}}{(2\pi N)^{2/3}}. \tag{6.10}$$

Here, $\mathbb{C}_c \approx 3.35 \times 10^{-3}$ is a coefficient set by the choice of envelope profile (6.8), c is defined in (4.17*c*) and $\Gamma = \sin\chi\cos^2(\chi/2)$. Figure 8(*b*) compares (6.10) with the

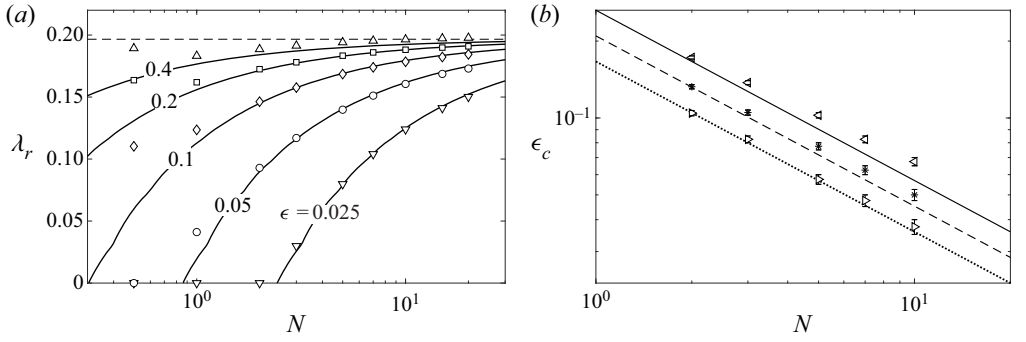

Figure 8. (*a*) Computed instability growth rates (in terms of the scaled time $T = \epsilon t$) according to the Floquet stability analysis as a function of N, the number of carrier wavelengths contained in the beam width, for the profile (6.9) with viscosity $\nu = 10^{-5}$, beam frequency $\omega = \sin 45^\circ$ and beam amplitudes $\epsilon = 0.025$ ($\triangledown$), 0.05 ($\circ$), 0.1 ($\Diamond$), 0.2 ($\square$) and 0.4 ($\triangle$). The corresponding asymptotic PSI growth rates, as predicted by (6.6), are overlaid and labelled. The PSI growth rate for a sinusoidal wave (i.e. $N \to \infty$) is indicated by the horizontal dashed line. (*b*) Minimum amplitude ϵ_c for instability as a function of N for $\nu = 5 \times 10^{-4}$ ($\triangleright$, dotted line), 10^{-3} ($*$, dashed line) and 2×10^{-3} ($\triangleleft$, solid line). Shapes correspond to Floquet analysis results while lines correspond to the amplitude threshold (6.10) predicted by the PSI theory.

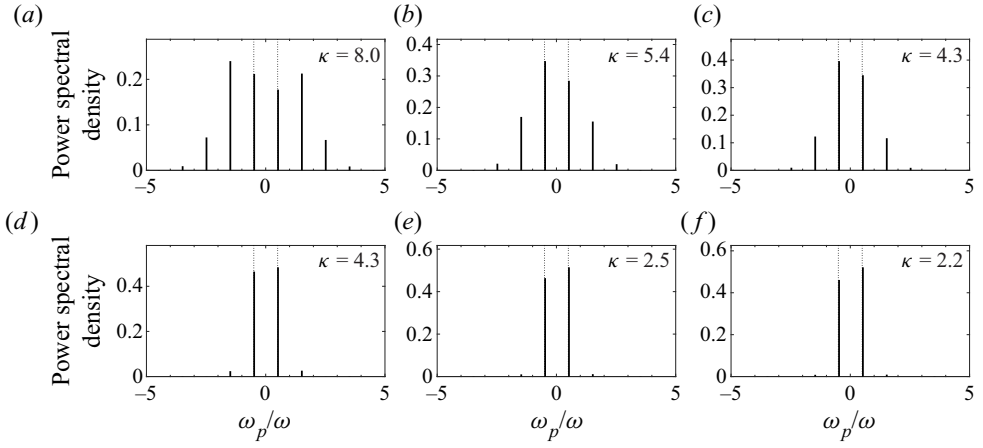

Figure 9. Time-frequency spectra of the fastest-growing Floquet mode for various configurations shown in figure 8(*a*). Panels (*a–c*) correspond to beam amplitude $\epsilon = 0.2$ and 0.05, respectively. Panels (*a*,*d*), (*b*,*e*) and (*c*,*f*) correspond to $N = 2$, 10 and 20, respectively. Vertical dotted lines in each plot correspond to the frequencies $\pm\omega/2$. The wavenumber κ for each mode is displayed.

minimum amplitude threshold found numerically using the Floquet analysis for various $2 \leq N \leq 10$ and for three different viscosities $\nu = 5 \times 10^{-4}, 10^{-3}$ and 2×10^{-3}. We observe excellent agreement between (6.10) and the numerical results.

Figure 9 plots the time-frequency spectra of the Floquet modes corresponding to the growth rates shown in figure 8(*a*) for $\epsilon = 0.05$ and 0.2, and for $N = 2$, 10 and 20. Similar to the results found in § 5.3 for near-inertial conditions, the frequency spectra widen as the beam amplitude ϵ is increased, corresponding to the emergence of multiple instability frequencies other than $\pm\omega/2$. When this happens, again we find that PSI theory, although it is no longer strictly valid, still provides accurate predictions of the instability growth rates.

Finally, it is worth noting that, according to (6.10), $\epsilon_c \to 0$ in the inviscid limit ($\nu = 0$) regardless of N. This hints that small-amplitude ($\epsilon \ll 1$) locally confined beams with general (not necessarily nearly monochromatic) profile are possibly susceptible to instability. This point is discussed below.

7. Broadband instability of small-amplitude beams

According to the asymptotic analysis of § 4, PSI of a small-amplitude ($\epsilon \ll 1$) beam of frequency ω involves fine-scale ($k \gg 1$) disturbances under the condition $\epsilon k \ll 1$, which ensures that the Floquet mode is dominated by the frequency components at $\pm\omega/2$. However, based on numerical solutions of the full Floquet stability eigenvalue problem, PSI theory continues to provide reliable predictions of instability growth rates when $\epsilon k = O(1)$ and the Floquet mode frequency spectrum becomes broadband (see figures 3, 5 and 6). This broadening of the frequency spectrum as ϵk is increased was also noted in the numerical computations of Onuki & Tanaka (2019) and it was attributed to the advection of the perturbation by the underlying-beam velocity field, an effect that has a passive role in regards to the instability growth rate. Here, we provide theoretical justification of this claim and also demonstrate that small-amplitude beams with general (not necessarily nearly monochromatic) locally confined profile may develop an essentially inviscid instability that features broadband frequency spectrum.

7.1. *Revised Floquet analysis*

Returning to the Floquet analysis in § 4, we adopt the frame riding with the primary wave

$$\xi' = \xi - \int^t \psi_{0\eta}\,\mathrm{d}t', \tag{7.1}$$

where $\psi_0 = O(\epsilon)$ is given by (4.3*a*). This key step (suggested by an anonymous referee) makes it possible to factor out the (along-beam) advection of the Floquet mode due to the underlying wave and thereby eliminate the $O(\epsilon k)$ terms in (4.11). Specifically, in view of (7.1), the Floquet mode in (4.4) and (4.10) is replaced by

$$\hat{\psi}'(\eta, t)\mathrm{e}^{\mathrm{i}\mu\xi'} = \mathrm{e}^{\lambda t}\mathrm{e}^{-\mathrm{i}\omega t/2}\exp(\mathrm{i}k(\eta\cos\chi - \xi'\sin\chi))\sum_{n=-\infty}^{\infty} A'^{(n)}(\eta)\mathrm{e}^{\mathrm{i}n\omega t}, \tag{7.2}$$

with similar expressions for $\hat{w}'$ and $\hat{\rho}'$. Substituting these revised modes into the linearized form of (4.1) and (4.2) governing the perturbations, and collecting equal harmonics leads to an infinite equation system, analogous to (4.11), for the amplitudes $\tilde{A}'^{(n)} = kA'^{(n)}$, $W'^{(n)}$ and $R'^{(n)}$ ($n = 0, \pm1, \pm2, \ldots$). Unlike (4.11), however, the coupling terms due to the interaction with the primary wave are now $O(\epsilon)$ instead of $O(\epsilon k)$. Thus, for $\epsilon \ll 1$, $k \gg 1$ and $\epsilon k = O(1)$, it is possible to asymptotically truncate the Fourier series in (7.2) and obtain a reduced stability eigenvalue problem for the dominant perturbation amplitudes.

In this new eigenvalue problem, the $O(\epsilon)$ instability growth rate derives from the $O(\epsilon)$ coupling of the perturbation with the primary wave, which now may be balanced with the $O(1/k)$ group velocity effect and the $O(\nu k^2)$ viscous dissipation. This 'distinguished limit' is achieved by the scalings

$$\lambda \to \epsilon\lambda, \quad \nu = \alpha'\epsilon^3, \quad k = \frac{\kappa'}{\epsilon}. \tag{7.3a–c}$$

Thus, compared with near-inertial PSI (cf. (5.2*a–d*)), here the growth rate is of the same order, but the perturbation length scale is shorter and the Reynolds number much higher.

Furthermore, although the Fourier series in (7.2) may be truncated, the Floquet mode as a whole features broadband frequency spectrum due to the factor $\exp(-\mathrm{i}k\xi'\sin\chi)$, which in view of (7.1) comprises all harmonics when $\epsilon k = O(1)$.

7.2. *Reduced eigenvalue problem*

We now sketch the derivation of the asymptotic stability eigenvalue problem appropriate to the limit $\epsilon \ll 1$, $k \gg 1$ and $\epsilon k = O(1)$. Upon implementing (7.3*a–c*), the equation system governing the Fourier amplitudes $\tilde{A}'^{(n)}$, $W'^{(n)}$ and $R'^{(n)}$, correct to $O(\epsilon)$, can be reduced to the following system for $\tilde{A}'^{(n)}$ ($n = 0, \pm1, \pm2, \ldots$):

$$\begin{aligned}
&\mathrm{i}(\Omega - n(n-1)\omega^2)\tilde{A}'^{(n)} \\
&\quad - \epsilon\left(\lambda\frac{\Omega + \left(n^2 - n + \frac{1}{2}\right)\omega^2}{\left(n-\frac{1}{2}\right)\omega} - \alpha'\kappa'^2\frac{f^2\cos^2\phi + \left(n-\frac{1}{2}\right)^2\omega^2}{\left(n-\frac{1}{2}\right)\omega}\right)\tilde{A}'^{(n)} \\
&\quad + 2\frac{\epsilon}{\kappa'}\left(\delta - \omega^2(n-1/2)^2\cos\chi\right)\frac{\mathrm{d}\tilde{A}'^{(n)}}{\mathrm{d}\eta} \\
&\quad - \epsilon(n-1/2)\,\omega\sin 2\chi\left(Q_{\eta\eta}\tilde{A}'^{(n+1)} + Q^*_{\eta\eta}\tilde{A}'^{(n-1)}\right) \\
&\quad + \epsilon\frac{n-\frac{1}{2}}{\omega}\sin\chi\left(\sin(\phi-\chi)\sin\phi + f^2\cos(\phi-\chi)\cos\phi\right) \\
&\quad \times\left(\frac{Q_{\eta\eta}\tilde{A}'^{(n+1)}}{n+\frac{1}{2}} - \frac{Q^*_{\eta\eta}\tilde{A}'^{(n-1)}}{n-\frac{3}{2}}\right) = O(\epsilon^2),
\end{aligned} \tag{7.4}$$

where Ω and δ are given in (4.17*a*) and (4.17*b*). Then, setting $\Omega = 0$ makes the $O(1)$ terms in (7.4) for $n = 0$, 1 drop out, and the dominant Fourier amplitudes $\tilde{A}'^{(0)}$ and $\tilde{A}'^{(1)}$ satisfy the closed system

$$\hat{\lambda}\tilde{A}'^{(0)} + \frac{c}{\kappa'}\frac{\mathrm{d}\tilde{A}'^{(0)}}{\mathrm{d}\eta} + \frac{\sin\chi}{\omega^2}\left(\delta + \frac{\omega^2}{2}\cos\chi\right)Q_{\eta\eta}\tilde{A}'^{(1)} = 0, \tag{7.5a}$$

$$\hat{\lambda}\tilde{A}'^{(1)} - \frac{c}{\kappa'}\frac{\mathrm{d}\tilde{A}'^{(1)}}{\mathrm{d}\eta} + \frac{\sin\chi}{\omega^2}\left(\delta + \frac{\omega^2}{2}\cos\chi\right)Q^*_{\eta\eta}\tilde{A}'^{(0)} = 0, \tag{7.5b}$$

where

$$\hat{\lambda} = \lambda + \alpha'\kappa'^2\beta, \tag{7.6}$$

with β and c given in (4.17*b*) and (4.17*c*). Equations (7.5) (along with the boundary conditions $\tilde{A}'^{(0)}, \tilde{A}'^{(1)} \to 0$ as $\eta \to \pm\infty$) define an eigenvalue problem for $\hat{\lambda} = \hat{\lambda}_r + \mathrm{i}\hat{\lambda}_i$. Here, in view of (7.6), $\hat{\lambda}_r$ may be interpreted as the inviscid instability growth rate whereas $\lambda_r = \hat{\lambda}_r - \alpha'\kappa'^2\beta$ accounts for the effect of viscous dissipation.

As remarked earlier, the instability described by (7.5) is distinct from PSI because the Floquet mode (7.2) features a broadband frequency spectrum and the scaling $\nu \propto \epsilon^3$ appropriate here requires larger Reynolds number than PSI, where $\nu \propto \epsilon^2$ according to (5.2*a–d*) and (6.4*a–d*). Therefore, as discussed in § 7.3, this broadband, essentially inviscid instability may affect beams that are not generally susceptible to PSI. Furthermore, the same type of instability replaces PSI under inviscid flow conditions in the limit where

the wavenumber of subharmonic perturbations is large enough so that $\kappa' = \epsilon k = O(1)$. For instance, at inertial conditions $\omega = 2f$, where according to (4.17) $\phi = 0$, $\delta = f^2 \cos\theta$, $\beta = 1$ and $c = 0$, (7.5) reduces to

$$2\hat{\lambda}\tilde{A}'^{(0)} + \tfrac{3}{4}\sin 2\theta Q_{\eta\eta}\tilde{A}'^{(1)} = 0, \tag{7.7a}$$

$$2\hat{\lambda}\tilde{A}'^{(1)} + \tfrac{3}{4}\sin 2\theta Q^*_{\eta\eta}\tilde{A}'^{(0)} = 0, \tag{7.7b}$$

which agrees with the limiting form, when $\kappa = \epsilon^{1/2}k = \kappa'/\epsilon^{1/2} \gg 1$, of the near-inertial PSI stability problem (5.3) at the critical frequency $\omega = 2f$ ($\hat{\sigma} = 0$). This explains why (5.3), which was derived under the assumption $\epsilon k \ll 1$, provides reliable predictions of instability growth rates even when $\epsilon k = O(1)$ and the Floquet mode is no longer dominated by the subharmonics at $\pm\omega/2$ (see figures 3, 5 and 6).

7.3. *Results for $f = 0$*

We now make a comparison of the predictions of the broadband-instability eigenvalue problem (7.5) with results from numerical Floquet analysis, under conditions where PSI is not expected to arise. Specifically, we consider again the beam with profile (3.1) and frequency $\omega = 0.1$ used in the discussion of near-inertial PSI of § 5 (see figure 1*b*), except here, we assume no background rotation ($f = 0$). In this instance, it follows from (2.3) that $\omega = \sin\theta$ so, making use of (4.17), $\sin\phi = \omega/2$, $\beta = 1/2$ and $\delta = \omega^2/2$. Thus, (7.5) and (7.6) take the form

$$\hat{\lambda}'\tilde{A}'^{(0)} + \frac{c}{\kappa'}\frac{\mathrm{d}\tilde{A}'^{(0)}}{\mathrm{d}\eta} + \sin\chi\cos^2\frac{\chi}{2}Q_{\eta\eta}\tilde{A}'^{(1)} = 0, \tag{7.8a}$$

$$\hat{\lambda}'\tilde{A}'^{(1)} - \frac{c}{\kappa'}\frac{\mathrm{d}\tilde{A}'^{(1)}}{\mathrm{d}\eta} + \sin\chi\cos^2\frac{\chi}{2}Q^*_{\eta\eta}\tilde{A}'^{(0)} = 0, \tag{7.8b}$$

where

$$\hat{\lambda} = \lambda + \tfrac{1}{2}\alpha'\kappa'^2, \tag{7.9}$$

with $c = \omega(2 - \cos\chi)/2$ and $\chi = \theta - \phi$. The eigenvalue problem (7.8) was solved numerically following the procedure used for (5.3). Here, the computational domain was varied between $\eta \in [-5, 5]$ and $[-75, 75]$, depending on the choice of κ', with a typical grid size of 3000 points.

Figure 10(*a*) compares the instability growth rates λ_r, as a function of the perturbation wavenumber k, predicted by the broadband-instability eigenvalue problem (7.8) and the numerical Floquet analysis for $\epsilon = 0.01$ under inviscid flow conditions ($\nu = 0$). We observe excellent quantitative agreement between the fully numerical and asymptotic instability growth rates. For comparison, the same figure also plots the growth rates for $f = 0.05$, corresponding to near-inertial conditions exactly at the critical frequency $\omega = 2f$. Figure 10(*a*) confirms that for $f = 0$, the beam is unstable when $\epsilon k \gtrsim O(1)$: the onset of instability occurs at $k \approx 45$ ($\epsilon k = \kappa' \approx 0.45$) and the growth rate keeps increasing monotonically, reaching a plateau for $k \gtrsim 300$ ($\epsilon k \gtrsim 3$). This is in contrast to the (near-inertial) instability for $f = 0.05$, which arises at a significantly lower value of $k \approx 10$ ($\epsilon k = 0.1$), consistent with the scaling $\kappa = \epsilon^{1/2}k = 1 = O(1)$ of near-inertial PSI, and has reached its plateau when $k \gtrsim 100$ ($\epsilon k \gtrsim 1$).

Figure 10(*b–d*) plots the frequency spectrum of the Floquet mode for $f = 0$ at $k = 80, 200$ and 400. Perhaps surprisingly, at $k = 80$ ($\epsilon k = \kappa' = 0.8$) the frequency components $\pm\omega/2$ are dominant so the spectrum is of the PSI type (figure 10*b*).

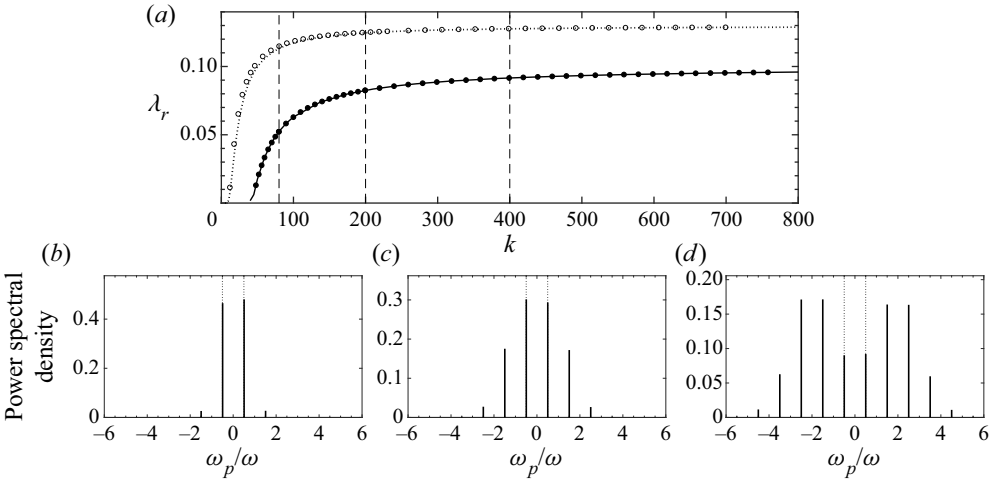

Figure 10. (*a*) Floquet growth rate (•) as a function of the perturbation wavenumber magnitude k using beam profile (3.1) for beam amplitude $\epsilon = 0.01$, primary beam frequency $\omega = 0.1$ and no background rotation ($f = 0$) under inviscid flow conditions ($\nu = 0$). Solid line corresponds to the asymptotic growth rate predicted by the broadband-instability eigenvalue problem (7.8). The Floquet growth rate for $f = 0.05$ (○) and the asymptotic near-inertial PSI growth rate (dotted line) predicted by the eigenvalue problem (5.3) are plotted for comparison. Vertical dashed lines indicate the values $k = 80$, 200 and 400. (*b*) Time-frequency spectra of the most unstable Floquet mode for $f = 0$ shown in panel (*a*) at $k = 80$. Vertical dashed lines indicate the frequencies $\omega_p = \pm\omega/2$. Panel (*c*) is the same as (*b*) but at $k = 200$ and panel (*d*) is the same as panel (*b*) but at $k = 400$.

However, the Floquet modes associated with the highest growth rates for $f = 0$ (which according to figure 10(*a*) are roughly 75 % of the highest near-inertial growth rates) are certainly broadband, as illustrated in figure 10(*c*,*d*) at $k = 200$ and 400, corresponding to $\epsilon k = \kappa' = 2$ and 4. These results indicate that the scaling argument made in § 4.2 (and KA14) for ruling out PSI of small-amplitude locally confined beams away from near-inertial conditions is not entirely binding: the dominant instability for $f = 0$ indeed is broadband, but PSI is still relevant near the onset of instability.

To examine the range of validity of the weakly nonlinear theory ($\epsilon \ll 1$) for broadband instability, in figure 11 we show a comparison of instability growth rates as predicted by (7.8) with numerical results obtained from Floquet analysis, for $\epsilon = 0.01$, 0.1 and 0.2 and two beam frequencies, $\omega = 0.1$ (figure 11*a*) and $\omega = 0.8$ (figure 11*b*). There is excellent quantitative agreement for $\epsilon \leq 0.1$, and the small-amplitude predictions remain reasonably accurate even for $\epsilon = 0.2$.

It was noted earlier that, in view of (7.3*a–c*), the broadband instability is expected to be more vulnerable to the effects of viscous dissipation than near-inertial PSI (cf. (5.2*a–d*)). This is illustrated in figure 12, which shows the effect of finite viscosity ($\nu = 10^{-7}$) on the instability growth rates for the same beam as in figure 10(*a*). Similar to inviscid flow conditions (figures 10*a* and 11), the asymptotic growth rates predicted by the broadband-instability eigenvalue problem (7.8) again show excellent agreement with the fully numerical results. For both $f = 0$ and $f = 0.05$ (i.e. near-inertial conditions), instability is suppressed when $k \gtrsim 110$ ($\epsilon k \gtrsim 1.1$), thereby eliminating the broadband-type instability and leaving only the PSI-type instability. As a result, instability is far weaker for $f = 0$ than for $f = 0.05$. Based on figure 12, for $\nu = 10^{-7}$, the maximum growth rate for $f = 0$ decreases by roughly 80 % relative to inviscid conditions, whereas the maximum growth rate for $f = 0.05$ decreases only by roughly 30 %.

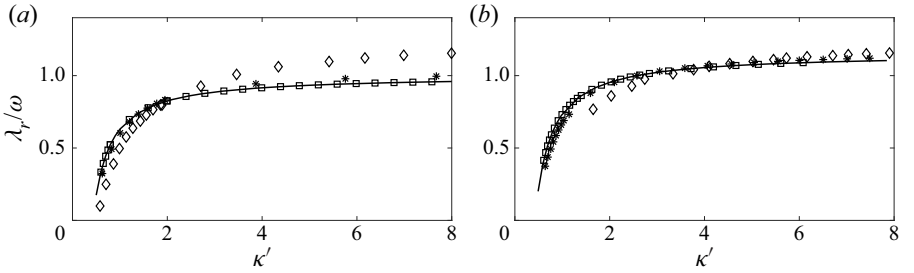

Figure 11. (*a*) Comparison of the instability growth rates λ_r, scaled by the beam frequency ω, predicted by the weakly nonlinear theory for broadband instability (solid lines) and the fully numerical Floquet analysis (shapes) for $f = 0$, $\nu = 0$ and beam profile (3.1). (*a*) Growth rates are plotted as a function of the scaled wavenumber parameter $\kappa' = \epsilon k$ for beam frequency $\omega = 0.1$ and amplitudes $\epsilon = 0.01$ (□), 0.1 (∗) and 0.2 (◇). Panel (*b*) is the same as panel (*a*) but for $\omega = 0.8$.

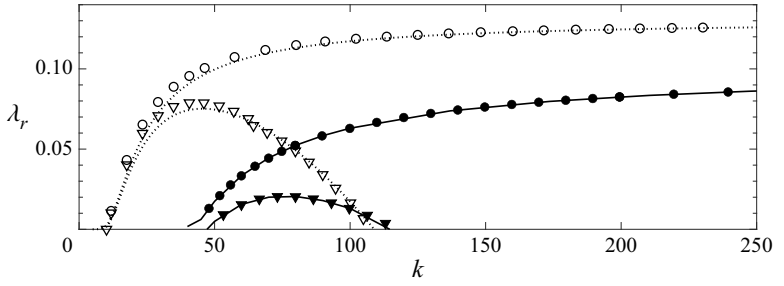

Figure 12. Effect of viscosity on the Floquet growth rates shown in figure 10(*a*) using the same beam profile (3.1), beam amplitude $\epsilon = 0.01$ and primary beam frequency $\omega = 0.1$, for $\nu = 10^{-7}$ (▲, △) and $\nu = 0$ (●, ○). Filled shapes (●, ▲) correspond to growth rates for $f = 0$, while open shapes (○, △) correspond to results for $f = 0.05$ (i.e. near-inertial conditions). The corresponding growth rates predicted by the near-inertial PSI eigenvalue problem (5.3) (dotted lines) and the broadband-instability eigenvalue problem (7.8) (solid lines) are overlaid.

8. Concluding remarks

We made an analytical and numerical study of instability mechanisms of small-amplitude finite-width internal gravity wave beams using a formal stability analysis based on Floquet theory. Our original motivation was to assess the validity of the approximate theories proposed in KA14 and KA17 for the PSI of small-amplitude beams. These models assume that PSI involves a resonant triad interaction between a beam of frequency ω and two fine-scale subharmonic perturbation wavepackets with carrier frequency $\omega/2$. This hypothesis is supported by our asymptotic analysis of the Floquet stability eigenvalue problem in the PSI regime, namely for a small-amplitude beam subject to fine-scale perturbations in the nearly inviscid limit. However, the Floquet instability mode also comprises two components with frequency $3\omega/2$, ignored in KA14 and KA17, which although they are smaller than the two subharmonic wavepackets, still play an important part, particularly in near-inertial PSI where they affect the instability growth rate.

After accounting for the $3\omega/2$ frequency components, the predictions of KA17 for near-inertial PSI of a locally confined beam are in excellent quantitative agreement with those of the Floquet stability analysis, even outside the formal range of validity of the approximate model. Close agreement is also found between the PSI model of KA14 and the exact linear stability analysis of nearly monochromatic beams away from

near-inertial conditions. In this instance, the $3\omega/2$ frequency components of the Floquet mode omitted in KA14 do not affect the PSI growth rate, which shows satisfactory agreement with that computed from the Floquet stability analysis even for a beam profile with as few as two carrier wavelengths. Furthermore, the validity of the minimum beam-amplitude threshold for PSI found in KA14 is confirmed.

An interesting insight provided by our analysis of the small-amplitude limit of the Floquet stability problem is that the coupling of the perturbation with the underlying beam is controlled by ϵk, where $\epsilon \ll 1$ measures the beam amplitude and $k \gg 1$ is the perturbation wavenumber. As a result, PSI arises only in the limit $\epsilon k \ll 1$ where the coupling is weak and the two subharmonic perturbation components with frequency $\omega/2$ dominate. This also explains why the frequency spectrum of the Floquet mode eventually becomes broadband as ϵk is increased. This broadening of the spectrum was also noted by Onuki & Tanaka (2019) and was attributed to the advection of the perturbation by the velocity field due to the underlying wave beam. We have confirmed this claim by formulating a Floquet stability analysis in the frame moving with the beam velocity. Furthermore, this revised Floquet analysis has brought out a new form of instability of small-amplitude beams, which arises for $\epsilon k = O(1)$ and involves broadband frequency spectrum. This essentially inviscid instability can impact beams with general (not necessarily nearly monochromatic) locally confined profile, which according to the scaling argument presented in § 4.2 (and KA14) are not susceptible to PSI away from near-inertial conditions.

Acknowledgements. The authors would like to thank the anonymous referees for providing insightful suggestions that greatly improved this work, particularly in § 7.

Funding. This work was supported in part by the US National Science Foundation under grant DMS-1512925 and a Graduate Research Fellowship (grant 1122374) to B.F.

Declaration of interests. The authors report no conflict of interest.

Author ORCIDs.
Boyu Fan https://orcid.org/0000-0002-1743-5225.

References

Bourget, B., Scolan, H., Dauxois, T., Le Bars, M., Odier, P. & Joubaud, S. 2014 Finite-size effects in parametric subharmonic instability. *J. Fluid Mech.* **759**, 739–750.

Cole, S.T., Rudnick, D.L., Hodges, B.A. & Martin, J.P. 2009 Observations of tidal internal wave beams at Kauai Channel, Hawaii. *J. Phys. Oceanogr.* **39** (2), 421–436.

Fan, B. 2020 Instabilities of finite-width internal wave beams. PhD thesis, Massachusetts Institute of Technology.

Fan, B. & Akylas, T.R. 2020 Finite-amplitude instabilities of thin internal wave beams: experiments and theory. *J. Fluid Mech.* **904**, A16.

Fan, B., Kataoka, T. & Akylas, T.R. 2018 On the interaction of an internal wavepacket with its induced mean flow and the role of streaming. *J. Fluid Mech.* **838**, R1.

Fovell, R., Durran, D. & Holton, J.R. 1992 Numerical simulations of convectively generated stratospheric gravity waves. *J. Atmos. Sci.* **49** (16), 1427–1442.

Gerkema, T., Lam, F.-P. & Maas, L.R.M. 2004 Internal tides in the Bay of Biscay: conversion rates and seasonal effects. *Deep-Sea Res.* II **51** (25–26), 2995–3008.

Hibiya, T., Nagasawa, M. & Niwa, Y. 2002 Nonlinear energy transfer within the oceanic internal wave spectrum at mid and high latitudes. *J. Geophys. Res.* **107** (C11), 3207.

Jamin, T., Kataoka, T., Dauxois, T. & Akylas, T.R. 2021 Long-time dynamics of internal wave streaming. *J. Fluid Mech.* **907**, A2.

Johnston, T.M.S., Rudnick, D.L., Carter, G.S., Todd, R.E. & Cole, S.T. 2011 Internal tidal beams and mixing near monterey bay. *J. Geophys. Res.* **116**, C03017.

JOUVE, L. & OGILVIE, G.I. 2014 Direct numerical simulations of an inertial wave attractor in linear and nonlinear regimes. *J. Fluid Mech.* **745**, 223–250.

KARIMI, H.H. & AKYLAS, T.R. 2014 Parametric subharmonic instability of internal waves: locally confined beams versus monochromatic wavetrains. *J. Fluid Mech.* **757**, 381–402.

KARIMI, H.H. & AKYLAS, T.R. 2017 Near-inertial parametric subharmonic instability of internal wave beams. *Phys. Rev. Fluids* **2** (7), 074801.

KATAOKA, T. & AKYLAS, T.R. 2015 On three-dimensional internal gravity wave beams and induced large-scale mean flows. *J. Fluid Mech.* **769**, 621–634.

LAMB, K.G. 2004 Nonlinear interaction among internal wave beams generated by tidal flow over supercritical topography. *Geophys. Res. Lett.* **31** (9), L09313.

MACKINNON, J.A. & WINTERS, K.B. 2005 Subtropical catastrophe: significant loss of low-mode tidal energy at 28.9°. *Geophys. Res. Lett.* **32** (15), L15605.

MIED, R.P. 1976 The occurrence of parametric instabilities in finite-amplitude internal gravity waves. *J. Fluid Mech.* **78** (4), 763–784.

MOWBRAY, D.E. & RARITY, B.S.H. 1967 A theoretical and experimental investigation of the phase configuration of internal waves of small amplitude in a density stratified liquid. *J. Fluid Mech.* **28**, 1–16.

ONUKI, Y. & TANAKA, Y. 2019 Instabilities of finite-amplitude internal wave beams. *Geophys. Res. Lett.* **46**, 7527–7535.

SONMOR, L.J. & KLAASSEN, G.P. 1997 Toward a unified theory of gravity wave stability. *J. Atmos. Sci.* **54** (22), 2655–2680.

STAQUET, C. & SOMMERIA, J. 2002 Internal gravity waves: from instabilities to turbulence. *Annu. Rev. Fluid Mech.* **34** (1), 559–593.

TABAEI, A. & AKYLAS, T.R. 2003 Nonlinear internal gravity wave beams. *J. Fluid Mech.* **482**, 141–161.

THOMAS, N.H. & STEVENSON, T.N. 1972 A similarity solution for viscous internal waves. *J. Fluid Mech.* **54**, 495–506.

YAU, K.H., KLAASSEN, G.P. & SONMOR, L.J. 2004 Principal instabilities of large amplitude inertio-gravity waves. *Phys. Fluids* **16** (4), 936–951.

YEH, K.C. & LIU, C.H. 1981 The instability of atmospheric gravity waves through wave-wave interactions. *J. Geophys. Res.* **86** (C10), 9722–9728.

YOUNG, W.R., TSANG, Y.-K. & BALMFORTH, N.J. 2008 Near-inertial parametric subharmonic instability. *J. Fluid Mech.* **607**, 25–49.